minerals

MDPI

Article

Geological and Geochemical Indicators of Lithium Prospectivity in Northern Gondwana Sedimentary-Basin Brines

Waleed Saeed *, Serguey Arkadakskiy and Saleh Alqahtani

Saudi Aramco, Dhahran 31311, Saudi Arabia; serguey.arkadakskiy@aramco.com (S.A.); saleh.qahtani.20@aramco.com (S.A.)
* Correspondence: waleed.saeed@aramco.com

Abstract

Sedimentary-basin brines are increasingly evaluated as unconventional lithium (Li) resources, but legacy datasets commonly lack Li measurements, hindering regional assessments. This study resolves this data deficit in the Northern Gondwana Region (NGR) by integrating archived hydrochemical and stable isotope data from Triassic, Jurassic, and Paleogene carbonate-hosted aquifers with global analogues. Major ions reveal high-salinity Na-Cl fluids (TDS = 84.9–328.0 g/L). Cl^-/Br^- mass ratios show deep Mesozoic brines track seawater evaporation as pristine, connate fluids, whereas the shallower Paleogene aquifer reflects meteoric flushing. Isotopic systematics ($\delta^{18}O$ up to +11.7‰) and aqueous geothermometers indicate paleotemperatures of >200 °C in the Mesozoic suites, severely transcending background conductive geotherms (117–134 °C). This anomaly indicates an open-system plumbing architecture where upwelling hydrothermal fluids aggressively leached incompatible elements from underlying syn-rift basal clastics. Synthesizing these mechanisms, we developed a multi-criteria screening framework based on four indicators: salinity regime, evaporative intensity, lithological source architecture, and hydrothermal signatures. Validation suites yield robust cross-basinal binary linear correlations between fluid equilibration paleotemperatures and absolute Li concentrations confirming thermal regimes as a primary thermodynamic control on Li mobilization. Validated against these global datasets, this predictive toolkit accurately isolates high-prospectivity targets (Triassic and Jurassic) from unmineralized horizons (Paleogene), offering an advanced front-end de-risking mechanism to optimize exploration and unlock critical mineral frontiers in global carbonate–evaporite basins.

Keywords: lithium prospectivity; basinal brines; Northern Gondwana; hydrothermal leaching; solute geothermometry; stable isotopes

Check for updates

Academic Editors: Zhixuan Han and Bimin Zhang

Received: 27 August 2026
Revised: 29 October 2026
Accepted: 5 November 2026
Published: 19 November 2026

Copyright: © 2026 by the authors. Licensee MDPI, Basel, Switzerland. This article is an open access article distributed under the terms and conditions of the Creative Commons Attribution (CC BY) license.

1. Introduction

Lithium (Li) is a critical element that has emerged over the past decade as an essential component of sustainable energy technologies. Traditionally, Li has been sourced from conventional mining operations, primarily from spodumene-bearing pegmatites [1] and continental surface brines, most notably within the South American Andean salars [2]. More recently, deep subsurface aquifers within sedimentary basins have emerged as a significant frontier in Li exploration [3]. The development of these unconventional resources stands to benefit substantially from decades of accumulated geological knowledge, extraction technologies, and infrastructure established by the hydrocarbon and geothermal industries [4].

Residual evaporitic brines can retain syngenetic Li introduced during sediment deposition or burial. Furthermore, Li can be actively concentrated in pore waters and sedimentary basin brines through various primary sources and epigenetic geochemical mechanisms (Figure 1). These processes include volcanic inputs, deep water–rock interactions, and the maturation of organic matter [3,5–12], the mechanisms of which are detailed in Section 2. While Li typically exhibits conservative behavior and remains dissolved during brine evolution, its accumulation can be sequestered or limited by uptake into authigenic clays and other secondary minerals [13].

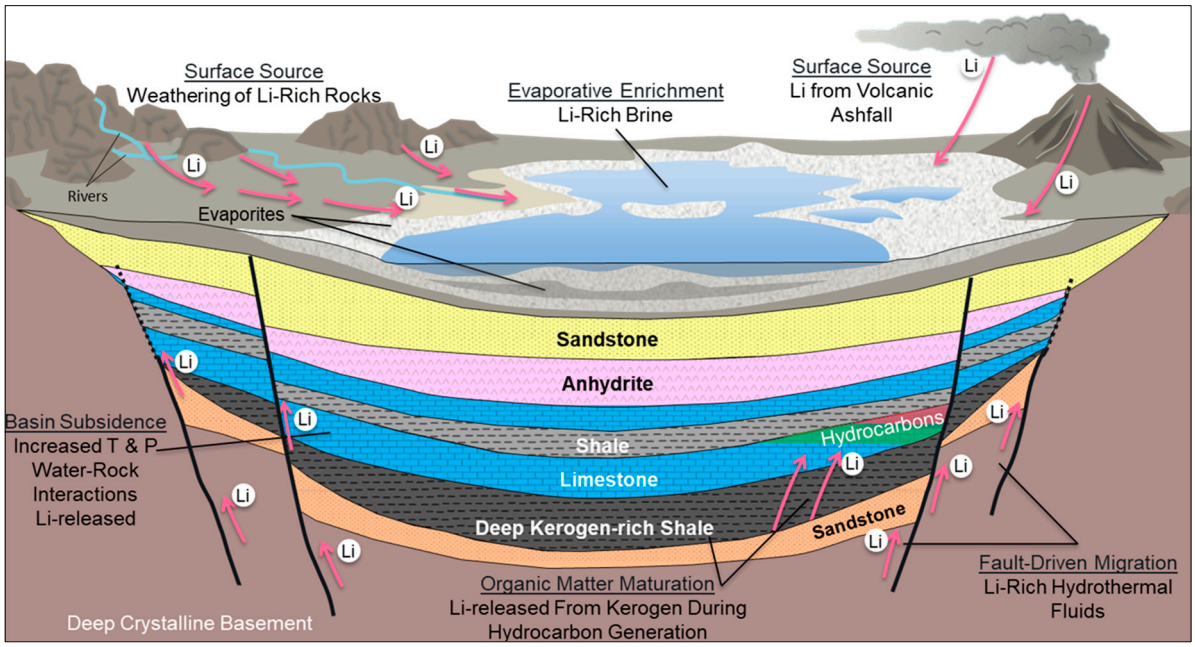


Figure 1. A schematic diagram depicting surface and subsurface processes for lithium (Li) introduction and enrichment in sedimentary basin brines. Arrows indicate plausible Li transport pathways: in solution, by ashfall, or in eroded detritus. Black heavy lines represent faults. The figure is constructed based on reviewed literature [3,5–12].

Despite the extensive historical characterization of many sedimentary basins, routine oilfield brine assays rarely include Li quantification, creating a critical data gap in regional prospectivity assessments. To address this deficiency, the present study pursues a threefold objective: (1) to synthesize the geochemical processes governing the mobilization and enrichment of Li in sedimentary brines; (2) to establish a conceptual framework of geological, hydrogeological, and geochemical indicators that correlate with Li enrichment; and (3) to evaluate the relationship between Li concentrations and routinely reported water chemistry parameters through a comparative analysis of global brine suites.

This workflow is applied to the Northern Gondwana Region (NGR), encompassing North Africa, Arabia, and parts of Iran, where extensive exploration for hydrocarbons has yielded vast datasets of subsurface brine chemistry. Given the existing infrastructure and mature geological models in the region, the NGR presents a significant target for Li exploration. The central objective of this study is to determine whether these deep basinal brines possess the requisite geochemical signatures and geological boundary conditions to support substantial Li accumulations.

2. Sources and Enrichment Mechanisms of Li in Sedimentary Brines

2.1. Primary Li Sources

The initial enrichment of sedimentary basin brines requires the liberation of Li into the aqueous phase via volcanism, the weathering of crystalline rocks, and the diagenetic leaching of clay-rich sediments (Figure 1). Lithium can be introduced directly into surface aqueous systems by volcanic aerosols and ash derived from highly evolved felsic (e.g., rhyolitic) eruptions. The efficacy of this mechanism is governed by the primary Li concentration of the volcanic protolith, the spatial distribution between the volcanic source and depocenter, eruptive explosivity, atmospheric transport dynamics, and ash particle-size distribution [14].

Over geological timescales, the subaqueous weathering of volcanic ash and pyroclastic material generates authigenic clay minerals, including kaolinite, smectite, and montmorillonite [3]. This alteration pathways can concurrently release Li from the glassy volcanic matrix and sequester it within secondary clay phases; subsequent desorption or structural release depends on whether Li occupies exchangeable interlayer sites or is incorporated into the octahedral sheets [5,15].

Additionally, Li is highly enriched in incompatible-element-rich, highly fractionated intrusive felsic rocks, such as peraluminous granites and granitic pegmatites, hosting minerals such as spodumene, lepidolite, petalite, and Li-bearing tourmaline [15]. Meteoric weathering and low-temperature alteration release aqueous Li ions from these mineral lattices and felsic-derived clastic sediments into surface and groundwater networks [16].

In strongly anoxic depositional environments, Li can be organo-complexed or structurally sequestered within organic matter in black shales and organic-rich mudstones [5,6,8,10]. The capacity of organic matter to host Li is primarily controlled by the total organic carbon (TOC) content, kerogen maceral type, and the specific nature of mineral–organic associations [8]. Furthermore, hydrous-pyrolysis experiments on organic-rich mudrocks demonstrate that organic matter macromolecular structure and mineral matrix associations significantly influence reaction kinetics and thermal cracking windows, thereby dictate the timing of elemental release [8]. This kerogen–Li coupling is supported by quantitative basin-scale numerical simulations of petroleum source-rock systems, which model the mass transfer of Li during kerogen catagenesis and its subsequent accumulation in co-produced brines [8]. Such simulations replicate Li concentrations in source-rock pore waters up to 430 ppm, matching empirical data from known Li-rich basinal fluids, and identify the Li stoichiometry of the kerogen decomposition reaction as the most critical parameter governing solute generation potential. This indicates that with increasing burial temperature, kerogen maturation and the subsequent expulsion of hydrocarbons trigger the liberation of this organo-bound Li into basinal pore fluids [6,8,10]. Consequently, the desorption and release of Li from organic complexes operate in tandem with the synchronous dehydration and structural transformation of associated clay minerals, as both mechanisms are fundamentally driven by burial thermobaric regimes [8].

2.2. Water–Rock Interaction and Diagenetic Processes

Water–rock interaction represents the primary mechanism for downstream Li enrichment via desorption, ion exchange, hydrothermal leaching, and incongruent mineral dissolution. The thermodynamic efficiency of these processes is tightly coupled to the thermobaric evolution of the sedimentary basin. In most basinal systems, the transition from near-surface regimes to deep burial environments ($T \approx 50$–150 °C) significantly accelerates reaction kinetics and enhances the solubility of Li-bearing mineral phases [9].

At low temperatures ($T < 50$ °C), Li partitioning is dominated by reversible cation exchange on clay surfaces. However, as burial depth increases, the thermal evolution of

the basin drives the diagenetic illitization of smectite, which acts as a critical juncture for Li redistribution [5,9,17]. This mineralogical transition, typically occurring between 60 °C and 120 °C depending on kinetic constraints and K+ activity, results in the expulsion of structurally bound Li from the octahedral sheets of smectite into the interstitial pore waters. While the exact mass-balance of Li release is highly lithology-dependent, this diagenetic purging can elevate the Li concentration of the aqueous phase by several orders of magnitude, transforming a baseline brine into an enriched system.

In higher-temperature hydrothermal regimes (T > 150 °C), the solubility of Li-bearing silicate matrices increases markedly, and reaction kinetics become strongly governed by the fluid-to-rock ratio. Elevated fluid flux through active fracture corridors maximizes the reactive surface area and maintains sub-saturation states, thereby sustaining the continuous leaching of Li from the host rock [18]. Consequently, the net solute budget within the aqueous phase is a combined function of fluid residence time and the peak temperatures sustained during the basin's thermal history.

2.3. Advective Transport and Fluid Migration

Fault and fracture corridors serve as primary structural conduits for vertical, advective fluid flow in the subsurface under favorable stress regimes and elevated pore-fluid pressures [19,20]. In numerous sedimentary basins, these deformational networks are interpreted to originate from or be reactivated by basement-involved tectonics, which enhances basement rock permeability [21] and establishes pathways for the ascending migration of hydrothermal fluids (including Li-rich fluids) from deep crystalline basements into shallower, permeable sedimentary units [22–24]. Because deep-seated fluids are driven by steep hydraulic and thermal gradients [25], the existence of regional-scale fault and fracture networks can not only elevate pre-existing Li concentrations but also introduce significant solute loads into previously depleted or pristine basinal brines.

Conversely, structural faults do not act exclusively as fluid conduits. Depending on the prevailing paleostress field, the clay volume within the fault core, and the degree of syn-deformational cementation or fault-gouge development, these features can act as absolute seals to cross-fault fluid flow, compartmentalizing reservoir aquifers and restricting vertical fluid migration [26]. In such structurally closed domains, Li-bearing fluids may become stratigraphically or structurally trapped beneath or lateral to sealing faults, or isolated within discrete fault-bounded compartments, rather than distributing uniformly throughout the basin. The net influence of a given fault network on Li redistribution is therefore governed by the dynamic interplay between its intrinsic permeability structure, its orientation relative to the contemporary stress field, and the regional hydrogeological framework. This dual conduit–barrier behavior must be carefully evaluated when appraising the prospectivity of faulted basins, as the specific structural architecture ultimately dictates whether advective pathways facilitate or restrict regional Li accumulation.

3. Geological Setting of the NGR in Relation to Potential Li Enrichment

The NGR possesses a complex geological history dating back to the Pan-African Orogeny and formation of Neoproterozoic basement from amalgamated cratons and juvenile crustal terranes [27] (Figure 2a), which was followed by (and partly overlapped with) extensional collapse and transcurrent faulting [28]. Peneplanation preceded the formation of a Paleozoic, dominantly clastic, platform followed by a Mesozoic, dominantly carbonate–evaporitic, platform that were straddled by several large sedimentary basins [29,30]. These basins formed along largely passive margins, but the sedimentary deposition was at times affected by periods of intra-plate or plate boundary-related structuration. The geological settings of the NGR fostered extensive, highly saline aquifer systems [31–34]. Widespread

halite and anhydrite units serve as indicators of past arid climates and high evaporation within these basins [30,35–37].

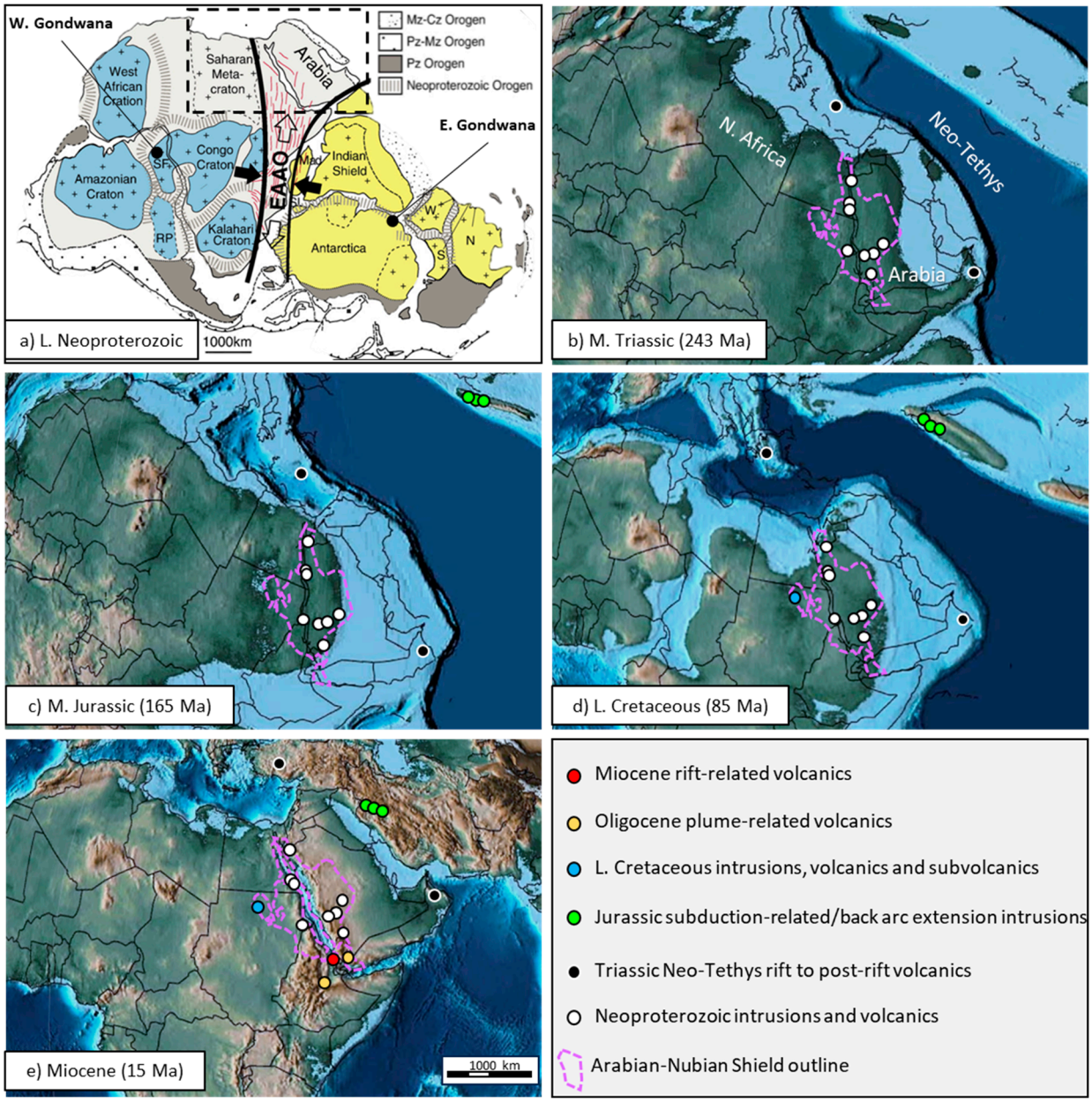


Figure 2. A panel showing the position and state of the NGR through time. (**a**) Late Neoproterozoic basement cratons and terranes amalgamation [27]. Dashed box shows the position of the NGR. (**b**–**e**) Mesozoic–Cenozoic paleogeographic maps from the PALEOMAP PaleoAtlas [38] viewed on GPlates [39]. The small circles in b-e are volcanic and intrusive units of different ages (see legend and text for more details): Neoproterozoic [40–43], Triassic [44,45], Jurassic [46], Late Cretaceous [47], and Miocene and Oligocene [48]. The reconstruction is shown here only as a visualization of the locations of different rocks discussed in the text during and after their formation.

The following sub-section provides a review of magmatic events that can potentially result in the formation of primary sources of Li, prior to incorporation into sedimentary brines. The section does not exhaustively cover the tectonic and magmatic histories of the region, but focuses mostly on events and rocks indicative of highly fractionated magmas prone to host high Li content. The locations of these events are shown in Figure 2 within the plate-scale paleogeographic reconstructions of [38].

3.1. Potential Primary Sources of Li in the NGR

The Neoproterozoic basement contains highly fractionated granites and granitic pegmatites [40]. In the Arabian-Nubian Shield (ANS), the Asir Terrane reports Li measurements of 4727–7865 ppm, primarily from lepidolites [41], while other regions feature plumasitic-type, highly evolved, leucocratic alkali-feldspar granites [42]. On the African side, Late Ediacaran Li–F albite granites in the Egyptian Eastern Desert host Li within zinnwaldite, Li-muscovite, and associated greisens [43].

Middle–Late Triassic high-silica A-type rhyolites in central Anatolia are interpreted as rift-related magmatism on the northern Gondwana margin during the opening of the southern Neo-Tethys and Inner-Tauride Ocean [44]. These rhyolites are strongly enriched in Rb, Nb, Ta and Sn, which marks them as highly evolved melts. Towards the southeast, Middle–Late Triassic trachytes and rhyolites occur as minor components of a dominantly alkali-basaltic sequence in the Oman Mountains, interpreted as post-breakup intraplate magmatism on the Arabian margin of the southern Neo-Tethys [45]. The rhyolites are strongly enriched in Zr, Nb, Y and REE with a negative Eu anomaly, indicating highly evolved alkaline melts.

Jurassic magmatism in the Sanandaj–Sirjan Zone, generally linked to the onset of Neo-Tethyan subduction (e.g., [46]) although an extensional origin has also been proposed [49], produced peraluminous S-type granites, syenogranites, and associated pegmatites, beside other intrusive rocks [46]. During this time, plate reconstruction models show near maximum extent of the Neo-Tethys Ocean separating the Cimmerian blocks (where the magmatism took place) from the Gondwana. Therefore, the potential contribution to Li content in the sedimentary units and brines would be limited to the Cimmerian side.

Late Cretaceous volcanic and subvolcanic magmatism occurred in the Nubian Desert and included mafic and felsic components [47]. The latter include trachytes, phonolites, ignimbrites and rhyolitic dykes and syenitic intrusions, and were interpreted to include peraluminous and peralkaline rocks.

Later, Oligocene plume-related volcanism produced bimodal lava flows and tuffaceous rocks in Yemen, and trachyte and rhyolitic ignimbrite at the Ethiopian escarpment of Afar, while Miocene syn-rift magmatism in Afar produced peralkaline rhyolites and alkali granites [48]. If Li-rich, the resulting rocks would only contribute leachable Li to Oligocene-Miocene rift basins.

Beyond primary igneous deposits, weathering and transport of Li-rich detritus eroded from exhumed intrusive rocks and volcanics into sedimentary basins can enable Li leaching into basinal brines during burial (as suggested for the ANS by Ortiz and Vahrenkamp [50]). Highly fractionated intrusive and subvolcanic rocks could also feed volcanic components that could reach sedimentary basins more directly.

3.2. Fault-Related Fluid Flow Examples in the NGR

Subsurface fluid distribution is strongly influenced by fault and fracture corridors that can act as primary conduits for vertical fluid migration [20]. Several structural, geochemical and petrographic studies showcase examples of fluid flow along faults from the NGR. For example, in a Late Triassic reservoir from Arabia, saddle dolomites indicate circulation of hot brines (≈160 °C) along faults [51]. Additionally, dolomitization trends of a Jurassic carbonate reservoir correlate with fault and fracture trends [52,53], interpreted as a result of dolomitizing fluids moving along these structures [52].

Al-Hajeri et al. [54] used fluid inclusion data integrated with seismic interpretation to conclude that rapid migration of hot fluids ($T > 200$ °C) from basement to Cretaceous reservoirs had probably occurred via deep-seated fault systems. Similar conclusions were reached for hydrocarbons flow, where variations in oil and gas source signatures and matu-

rities, integrated with seismic interpretation, strongly suggested preferential, fault-related, fluid flow [55]. Taken together, these examples indicate that the NGR is characterized by a plumbing system capable of transporting deep-sourced fluids.

4. Materials and Methods

4.1. Data Selection and Database Compilation

This study integrates primary archived hydrochemical data from three deep, carbonate-hosted aquifers within the NGR with a comprehensive global compilation of published sedimentary basin brine datasets. The studied aquifers are characterized by predominantly carbonate lithologies interspersed with thick evaporite sequences and underlain by basal siliciclastic successions. The primary dataset comprises representative formation water samples collected from the Triassic ($n = 6$), Jurassic ($n = 4$), and Paleogene ($n = 4$) stratigraphic intervals. Notably, within the Paleogene cohort, three samples represent deep baseline formation waters, whereas the fourth sample serves as a distinct hydrochemical reference representing a highly diluted basinal brine endmember, as evaluated in subsequent discussion sections. For comparative framework evaluation, public records of 9 NGR subsurface brines from close geological analogues—specifically carbonate–evaporite hydrocarbon reservoirs—were compiled across the Permo-Triassic [32] and Middle–Upper Jurassic sequence [34] (Table A1).

To establish a robust geochemical benchmark for deep basinal Li enrichment, public datasets from non-NGR basins were compiled based on strict geological and lithological analogy to the study area, focusing exclusively on carbonate-hosted reservoirs intimately associated with thick evaporite units. The compiled comparative dataset is organized chronostratigraphically, beginning with Paleozoic records from the Devonian strata of the Western Canada Sedimentary Basin ($n = 22$) [56] and the Devonian Dundee Limestone ($n = 6$) [57]. These are followed by Mississippian samples from the Charles Formation ($n = 25$), Lower Cretaceous samples from the Edwards Formation ($n = 6$) [57], and Upper Jurassic samples from the Smackover Formation ($n = 12$) [58] (Table A1).

4.2. Data Quality Control and Public Data Screening Protocols

For the primary NGR study aquifers, the analytical suite (Table 1) includes major aqueous ions (Na^+, K^+, Ca^{2+}, Mg^{2+}, Cl^-), along with minor elements (SO_4^{2-}, and HCO_3^-, Br^- and B). Total dissolved solids (TDS) concentrations were strictly calculated via the summation of these measured constituents. Stable water isotope values ($\delta^{18}O$ and δ^2H, reported in per mil [‰] relative to Vienna Standard Mean Ocean Water (VSMOW)) are provided in Table 1 to constrain fluid origins and mixing lines.

To ensure the geochemical integrity and reliability of the compiled public datasets, a rigorous multi-stage screening and verification protocol was implemented. First, a strict pH filter ($4.5 \leq pH \leq 10.5$) was applied to exclude any fluid samples potentially altered by drilling fluid contamination or post-perforation well-bore acidizing treatments, thereby isolating pristine formation waters. Second, a spatial consistency filter was enforced to ensure that any localized hydrochemical anomalies were cross-referenced and validated within their specific field, structural block, and formation contexts. Finally, to eliminate analyses with poor analytical precision or significant unmeasured ionic components, the charge-balance error (CBE) was calculated for each sample using standard equivalent concentrations. Only analyses yielding a CBE within a strict threshold of ±10% were accepted for subsequent geochemical modeling and comparative interpretation.

Table 1. Major and minor ion concentrations, and stable isotopic compositions of the brine samples from this study.

Age	pH	TDS	Ca	Mg	Na	K	HCO_3	Cl	SO_4	B	Br	CBE	Cl/Br	$^{18}O_{V\text{-}SMOW}$	$^{2}H_{V\text{-}SMOW}$
Unit		g/L	g/L	g/L	g/L	g/L	mg/L	g/L	mg/L	mg/L	mg/L	%	Mass Ratio	‰	‰
Triassic	5.9	230.9	13.2	1.82	65.6	13.38	341	132.9	343	558	2790	2.7	47.6	11.7	−20.0
	5.7	259.4	16.7	2.94	66.4	7.02	297	162.7	272	338	2720	−5.6	59.8	8.3	−19.5
	6.3	260.2	21.4	2.12	60.6	11.50	2025	159.0	721	586	2192	−4.4	72.5	9.4	−18.5
	6.3	266.5	22.3	2.20	63.1	11.88	661	162.9	768	582	2062	−3.4	79.0	9.8	−18.2
	6.1	260.5	22.0	2.16	61.5	11.61	448	159.3	742	568	2136	−3.4	74.6	9.5	−18.8
	6.1	315.2	26.3	2.49	85.2	12.65	464	184.6	410	550	2500	2.7	73.8	9.0	−19.0
Jurassic	4.9	328.0	35.2	1.63	80.8	14.55	246	192.0	319	571	2729	2.8	70.3	10.0	−12.8
	5.1	321.5	29.8	1.50	84.4	14.03	239	188.5	316	569	2116	2.6	89.1	9.9	−13.3
	5.4	323.6	18.8	1.20	93.7	14.53	265	191.7	421	557	2492	0.3	76.9	10.0	−17.1
	5.3	320.6	19.3	1.30	95.3	15.09	276	186.2	387	572	2338	2.8	79.6	9.8	−16.4
Paleogene	7.2	110.7	6.5	2.12	32.0	0.69	215	67.9	820	40	513	−0.9	132.4	−5.2	−40.4
	7.3	123.6	7.1	2.64	34.6	0.84	210	76.1	1602	38	555	−2.2	137.1	−2.4	−34.2
	6.2	84.9	5.4	1.46	24.9	0.42	578	51.1	757	24	348	0.4	147.0	−3.3	−45.9
	7.1	14.2	0.6	0.3	4.1	0.2	479	7.4	1036	5	55.2	−0.2	134.1	−6.8	−56.5

5. Results

5.1. Major and Minor Ion Chemistry

The comprehensive hydrochemical compositions of the analyzed NGR brines are presented in Table 1. The sampled formation waters exhibit slightly acidic to near-neutral characteristics, with a pH range spanning 4.9 to 7.3. The lowest pH values (4.9–5.4) are systematically restricted to the deep Jurassic reservoir horizons, whereas the highest values (6.2–7.3) characterize the shallower Paleogene aquifers.

Excluding the highly diluted Paleogene reference sample, the salinity of the formation waters varies distinctly across the three target aquifers. The Triassic brines exhibit TDS concentrations ranging from 230.9 to 315.2 g/L, the Jurassic brines display the highest and most tightly clustered salinity signature at 320.6 to 328.0 g/L, and the Paleogene baseline brines exhibit lower salinities between 84.9 and 123.6 g/L. A highly dilute Paleogene sample yielding a TDS of 14.2 g/L was also recorded; however, it is excluded from these primary baseline salinity ranges and is utilized specifically as a brackish/meteoric endmember to constrain fluid mixing trends in subsequent modeling chapters. Relative to a mean modern seawater baseline (TDS ≈ 35 g/L), these salinities correspond to empirical concentration factors of approximately 6.6–9.0 for the Triassic, 9.2–9.4 for the Jurassic, and 2.4–3.5 for the Paleogene suites.

The major ionic matrix across all aquifers is heavily dominated by ions Cl^- (51.1 to 192.0 g/L) and Na^+ (24.9 to 95.3 g/L). Among the alkaline earth divalent cations, Ca^{2+} concentrations display a wide variance from 5.4 to 35.2 g/L, showing strong enrichment in the deep Jurassic reservoirs, whereas Mg^{2+} remains relatively low and uniform (1.20 to 2.94 g/L). Dissolved K^+ content shows a striking contrast between the older and younger systems, being highly enriched in the Triassic and Jurassic brines (7.02 to 15.09 g/L) but significantly depleted in the Paleogene waters (0.42 to 0.84 g/L).

Minor and trace solutes also vary systematically by reservoir age. Dissolved HCO_3^- concentrations range from 210 to 2025 mg/L and SO_4^{2-} values range from 272 to 1602 mg/L. Total dissolved B and Br^- are strongly elevated in the Triassic and Jurassic systems (B: 338–586 mg/L; Br^-: 2062–2790 mg/L), while being significantly lower in the Paleogene baseline brines (B: 24–40 mg/L; Br^-: 348–555 mg/L).

5.2. Isotopic Composition of Basinal Fluids

The $\delta^{18}O$ and $\delta^{2}H$ signatures of the studied NGR fluids (Table 1) reveal a strong coupling between isotopic fractionation states and reservoir chronostratigraphy. A pronounced

isotopic contrast occurs between the Paleogene formation waters and those from the older Mesozoic successions.

The Paleogene baseline brines are markedly depleted, yielding δ^2H and $\delta^{18}O$ values that cluster between −45.9‰ and −34.2‰, and −5.2‰ to −2.4‰ (relative to VSMOW), respectively. In stark contrast, the deeper Triassic and Jurassic brines exhibit pronounced enrichment in both heavy isotopes. The Jurassic reservoir brines display highly restricted and enriched isotopic fields, with δ^2H ranging from −17.1‰ to −12.8‰, and $\delta^{18}O$ fixed between +9.8‰ and +10.0‰. The underlying Triassic brines preserve a similar enrichment trajectory but define a broader, more heterogeneous distribution, with δ^2H values spanning −20.0‰ to −18.2‰ and $\delta^{18}O$ ranging widely from +8.3‰ to +11.7‰.

6. Discussions

6.1. Evolution of Brine Salinity and Fluid Compartmentalization

Based on the distinct chemical and isotopic compositions detailed in the preceding sections, the analyzed NGR formation waters exhibit discrete salinity regimes that correlate tightly with reservoir chronostratigraphy. The Triassic and Jurassic sequences are characterized by highly concentrated, hyper-saline brines, whereas the Paleogene aquifers host substantially more diluted fluids. Despite these broad variances in TDS, all three distinct aquifer horizons display systematic solute evolution trends.

Evaluation of major ionic components to delineate hydrochemical facies reveals that, despite a carbonate-dominated reservoir matrix which typically promotes the development of Ca-Mg-HCO_3 or Ca-Mg-SO_4 water types, all baseline samples are heavily dominated by a Na-Cl facies (Figure 3). This pervasive Na-Cl signature indicates that the aggregate basinal salinity is driven by a highly saline fluid end-member rather than the simple in-situ congruent dissolution of the host carbonate matrix. This finding is fundamentally consistent with historical basinal fluids documented from regional Mesozoic and Cenozoic carbonate systems across the NGR [32,34,59]. However, while macro-classification captures the dominant ionic proportions, it does not preclude the subsequent thermodynamic modification of specific minor or trace components via fluid–rock exchange, localized diagenesis, or late-stage mixing.

The major mechanisms responsible for generating deep Na-Cl basinal salinities are the advanced subaerial evaporation of seawater and the subsurface incongruent dissolution of evaporitic halite, both of which can be rigorously distinguished utilizing solute Cl^-/Br^- mass ratios [60]. The conservative behaviors Cl^- and Br^- during low-to-moderate temperature basinal evolution provide a strict mathematical framework for reconstructing fluid provenance and tracking subsequent physical or chemical overprints. Specifically, the Seawater Evaporation Trend (SET) maps a highly predictable trajectory between these two ions; while fluids originating from the progressive evaporation of pristine seawater fall directly along this baseline, waters dominated by the dissolution of bedded halite plot significantly above it due to the strong exclusion of the larger Br^- ion from the halite crystalline lattice [60].

The discrete, completely non-overlapping Cl^-/Br^- weight ratio signatures observed among the three target systems—ranging from 47.6 to 79.0 for the Triassic, 70.3 to 89.0 for the Jurassic, and 132.3 to 146.8 for the Paleogene suites (Table 1)—provide robust chemical evidence that these stratigraphic intervals function as strictly isolated hydraulic compartments. This extensive compartmentalization is further validated by published companion strontium isotope ($^{87}Sr/^{86}Sr$) systematics. The highly disparate radiogenic strontium signatures recorded for the Permo-Triassic [61], Middle-to-Upper Jurassic [34], and Paleogene [31] reservoirs reflect distinct fluid–rock isotopic equilibration histories. This confirms the absence of significant regional, cross-formational fluid communication or

hydraulic leakage among these specific stratigraphic units, though it does not preclude the localized ascendancy of deep-seated, basement-derived hydrothermal fluids along isolated structural conduits into individual reservoirs.

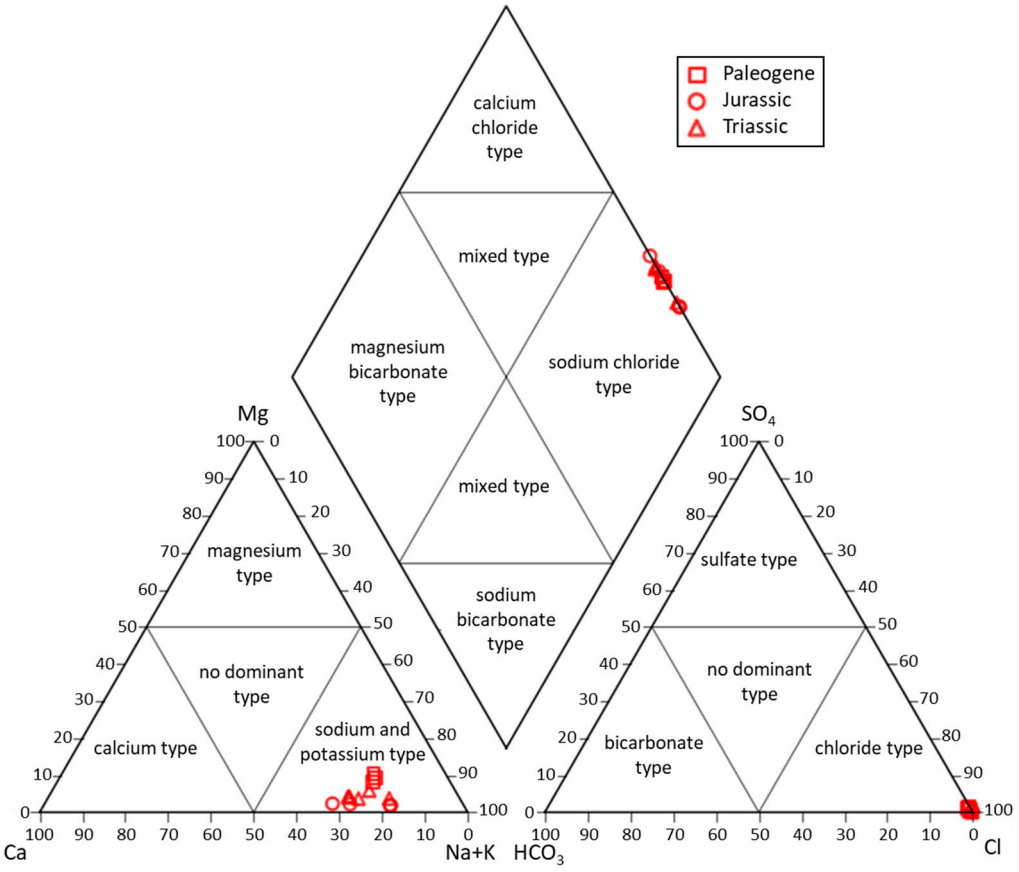


Figure 3. Piper diagram comparing the major ion chemistry of brine samples from the study brine aquifers. The diagram highlights the similarities in hydrochemical facies between these formations, with implications for the origin and evolution of the brines.

The distinctive evolutionary trajectories of these reservoirs reflect their isolated post-depositional histories. The Jurassic samples plot directly along the SET, away from saturation with halite (Figure 4). This specific positioning suggests that these basinal brines were derived from paleoseawater by an evaporative process that proceeded well into the halite stability field and reached near the stage of epsomite precipitation. Similarly, the underlying Triassic samples preserve a closely matched evolutionary history, plotting along and close to the SET. This shared alignment demonstrates that both Mesozoic fluid aquifers share a fundamentally similar trajectory rooted in advanced primary seawater evaporation. However, the underlying Triassic samples display a subtle but systematic negative offset slightly below the SET. While such relative bromide enrichments are occasionally attributed to syndepositional halite recrystallization cascades [60], the highly hydrocarbon-prolific nature of these Triassic carbonate units suggests an organic-derived bromine contribution is equally plausible. Specifically, the deep thermal cracking and degradation of organo-bromine complexes within kerogen matrices during peak oil and gas catagenesis [62] likely liberated non-marine Br^- directly into the interstitial pore waters, thereby lowering the baseline Cl^-/Br^- signature.

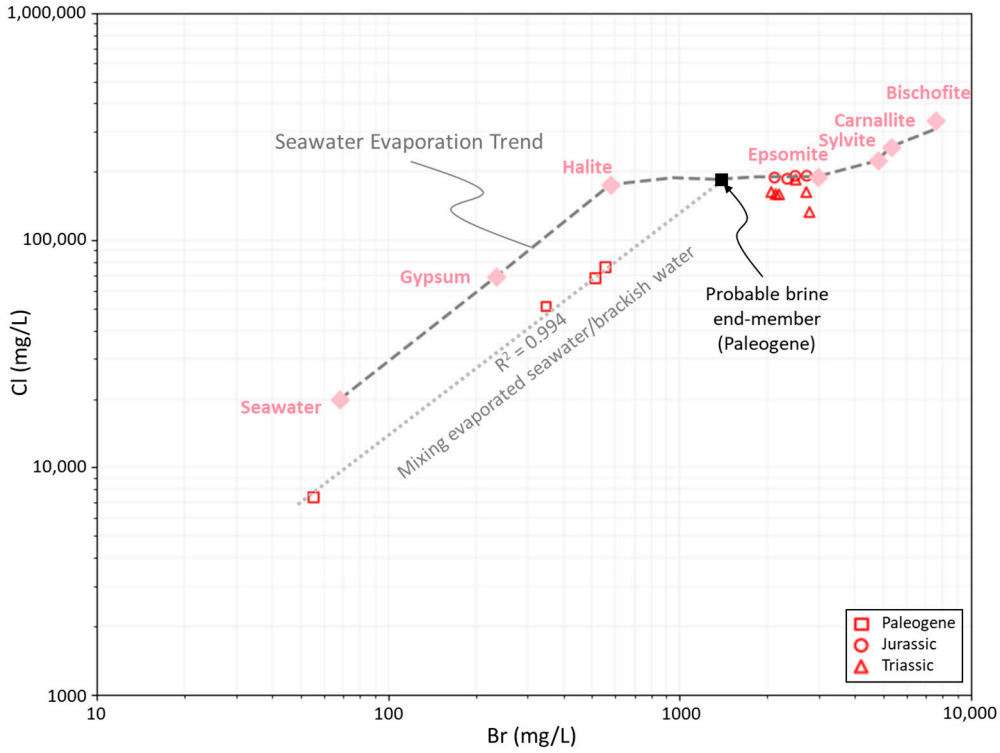


Figure 4. Logarithmic plot of Cl versus Br concentrations during seawater evaporation from Carpenter [60], illustrating the initial precipitation point of evaporite mineral phases (after [63]). The plot also shows possible mixing scenarios [64] with various halite dissolution products and end-member waters.

The shallower Paleogene aquifer exhibits a profound departure from the SET, plotting well within lower salinity regimes. The published presence of detectable radiocarbon (^{14}C) concentrations demonstrates a distinctly young modern or paleometeoric hydrodynamic component within the Paleogene system, highlighting the sweeping influence of paleometeoric recharge events during the Late Pleistocene and Early Holocene wet phases within an unconfined, hydrogeologically open regime [31]. The Cl^-/Br^- distribution of these Paleogene formation waters defines a remarkably tight linear dilution trajectory ($R^2 = 0.99$; Figure 4), anchored directly by the measured brackish endmember (TDS = 14.2 g/L). While the pristine, unmixed Paleogene brine endmember is no longer directly observable in the modern subsurface due to this flushing event, mathematical extrapolation of the regression vector back to its intersection with the SET allows for the accurate reconstruction of the primary evaporative chemistry of the paleoseawater prior to meteoric overprinting (Figure 4).

6.2. Hydrothermal Mobilization and Diagenetic Controls on Fluid Composition

To determine the specific mechanisms controlling metal and metalloid mobilization within the target aquifers, we evaluated the concurrent impacts of diagenetic mineral transformations and deep basinal thermal regimes. Following the chlorinity-normalization methodology of Mirnejad et al. [59], we assessed the relative enrichment or depletion of individual solutes relative to an evolved marine bittern fluid end-member. An empirical concentration factor was derived from the absolute Cl^- content of each sample relative to mean modern seawater [60], establishing the theoretical baseline abundances of elements expected within a strictly closed-system evaporative brine. Measured solute concentrations were subsequently normalized against these theoretical values to yield enrichment factors (EFs) that isolate selective chemical mobilization pathways (Figure 5).

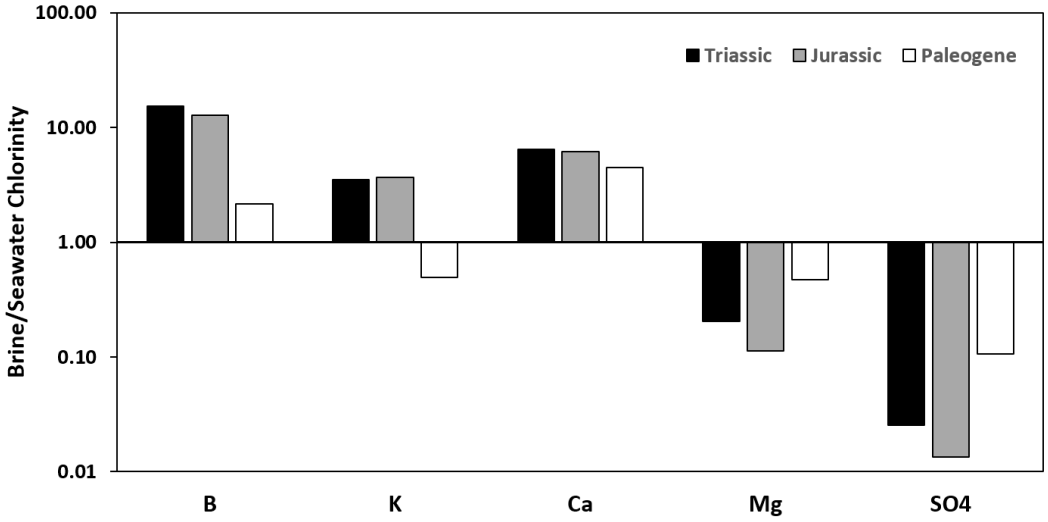


Figure 5. Elemental patterns of the study aquifer brines normalized to seawater chlorinity [60].

The resulting patterns demonstrate that B and K^+ are enriched within the Triassic and Jurassic suites, displaying EFs of 8.9–18.1 and 2.1–4.9, respectively. We propose that these marked geochemical anomalies are the direct product of high-temperature hydrothermal water–rock interaction. This interpretation is independently supported by the stable water isotope configurations. While the major ion vectors of the Triassic and Jurassic samples align with advanced seawater evaporation trends, they exhibit a prominent, decoupled enrichment in $\delta^{18}O$ without a corresponding vertical shift in $\delta^{2}H$ (Figure 6). This specific isotopic decoupling is a classic hallmark of high-temperature oxygen-isotope exchange between deep basinal fluids and rock-forming carbonate or silicate minerals under restricted fluid-flux conditions during deep burial or active hydrothermal circulation [65].

The magnitude of B enrichment, in particular, points to a paleothermal regime that significantly exceeded that of simple conductive burial. Linear conductive thermal modeling of the NGR—utilizing a regional surface temperature baseline of 27.2 °C and an average geothermal gradient of 28.5 °C/km [66]—yields a mean ambient conductive geotherm of approximately 117 °C for the Triassic aquifer (9984–13,690 ft) and 134 °C for the Jurassic aquifer (14,000–14,100 ft) (Table 2). Because the intensive leaching and breakdown of primary silicate frameworks typically require temperatures exceeding 150 °C [67], these background conductive values are thermodynamically insufficient to drive the observed B mobilization. To further constrain the basin's paleothermal architecture, we applied the solute geothermometry framework of Giggenbach [68], utilizing co-existing Na-K-Mg concentrations to estimate the temperature of deep water–rock equilibration.

Table 2. Geothermometric data for the brines in Paleogene, Jurassic, and Triassic aquifers.

Aquifer	Linear Conductive Modeling (°C)	Giggenbach [68] (Na-K) (°C)	Giggenbach [68] (K-Mg) (°C)
Paleogene	71	131	103
Jurassic	134	276	230
Triassic	117	283	203

As summarized in Table 2, the calculated geothermometric paleotemperatures significantly transcend the theoretical conductive ambient basinal geotherms. The Triassic aquifer exhibits average equilibration temperatures of 283 °C ($T_{Na\text{-}K}$) and 203 °C ($T_{K\text{-}Mg}$), while the Jurassic aquifer yields averages of 276 °C ($T_{Na\text{-}K}$) and 230 °C ($T_{K\text{-}Mg}$). In stark contrast, the shallower Paleogene aquifer preserves substantially lower values ($T_{Na\text{-}K} \approx 132$ °C and

$T_{K\text{-}Mg} \approx 103$ °C), which are fully consistent with its shallow burial depth and overprinting by recent meteoric recharge. The striking discrepancy between background conductive geotherms and the Giggenbach-derived temperatures for the Triassic and Jurassic intervals suggests that these deep Mesozoic aquifers were fundamentally influenced by hot, deep-seated hydrothermal fluids. While these elevated solute geothermometers and the marked $\delta^{18}O$ shifts provide strong supporting evidence for the circulation of anomalous, high-temperature fluids, we exercise appropriate scientific caution regarding the explicit physical mapping of subsurface structural features. Geochemical and isotopic anomalies function as direct indicators of fluid-flux history and paleothermal regimes rather than direct physical structural planes. Nevertheless, given the thick, regionally restrictive aquitards separating these deep Mesozoic reservoirs, the localized upwelling of such high-temperature fluids is difficult to reconcile via simple conductive or stratigraphically confined lateral flow. Therefore, the vertical upwelling of deep-seated fluids through deeply penetrating, basement-involved fault and fracture networks represents the most geologically plausible plumbing mechanism to facilitate this localized advective heat and solute transport.

Crucially, while this open-system advective framework clearly supplied the anomalous thermal energy and advective driving force required for regional metal mobilization, the relative contribution of primary solute sources remains open to two highly probable scenarios. First, the ascending hydrothermal fluids may have been inherently B-rich, transporting deep-seated basement solutes directly up along regional fault corridors. Second, the influx of these ultra-hot fluids may have acted as a thermal catalyst, driving the aggressive, high-temperature leaching of B directly from the thick, basal siliciclastic successions that structurally underlie the target carbonate reservoirs. Given the available geochemical data, both pathways represent highly viable mechanisms for introducing significant B, and potentially Li, loads into the basinal brine system, and they may operate either as independent or mutually reinforcing processes.

This diagenetic model is strongly supported by the coordinated mass-balance evolution of major divalent cations, specifically marked by pronounced Mg^{2+} depletion operating in tandem with Ca^{2+} enrichment. Chlorinity-normalization reveals Ca^{2+} enrichment factors of 6.4 and 6.2 for the Triassic and Jurassic aquifers, respectively, contrasted against depletions in Mg^{2+} (EF = 0.20 and 0.10, respectively). This distinct elemental signature indicates that pervasive subsurface dolomitization of the precursor limestone matrix systematically sequestered aqueous Mg^{2+} into the stabilizing carbonate lattice while synchronously liberating stoichiometric equivalent loads of Ca^{2+} into the migrating fluid:

$$2CaCO_3 + Mg^2 + \leftrightharpoons CaMg(CO_3)_2 + Ca^{2+} \quad (1)$$

Furthermore, the observed depletion of dissolved SO_4^{2-}, which falls well below conservative marine seawater evaporation benchmarks (Figure 5), is mechanically linked to the hydrothermal processes via two concurrent chemical sinks. First, the massive liberation of Ca^{2+} during hydrothermal limestone dissolution increased the total ionic activity product far beyond the solubility product of calcium sulfate [69], triggering the widespread subsurface precipitation of authigenic anhydrite. This mineralogical sink is structurally verified by the pervasive occurrence of late-stage anhydrite vein networks within deep reservoir core matrices. Second, the ubiquitous presence of dissolved H_2S across all analyzed Mesozoic aquifers indicates that a significant fraction of the remaining dissolved sulfate was consumed via thermochemical sulfate reduction (TSR), where SO_4^{2-} served as the primary terminal electron acceptor for the anaerobic, thermally driven oxidation of co-existing reservoir hydrocarbons.

In contrast, the shallow Paleogene aquifer (878–2209 ft) represents a geochemically immature, low-prospectivity horizon. Its marked depletion in both heavy stable isotope

signatures ($\delta^{18}O$ and $\delta^{2}H$) is fully consistent with a history dominated by extensive paleometeoric flushing events [31]. The high-volume influx of ambient, low-temperature surface-derived meteoric waters suppressed the thermal evolution of the reservoir, preventing the system from achieving the critical thermodynamic activation thresholds required to trigger deep silicate framework leaching. Consequently, this hydrogeological regime resulted in a highly conservative, un-enriched geochemical profile devoid of significant critical metal accumulation.

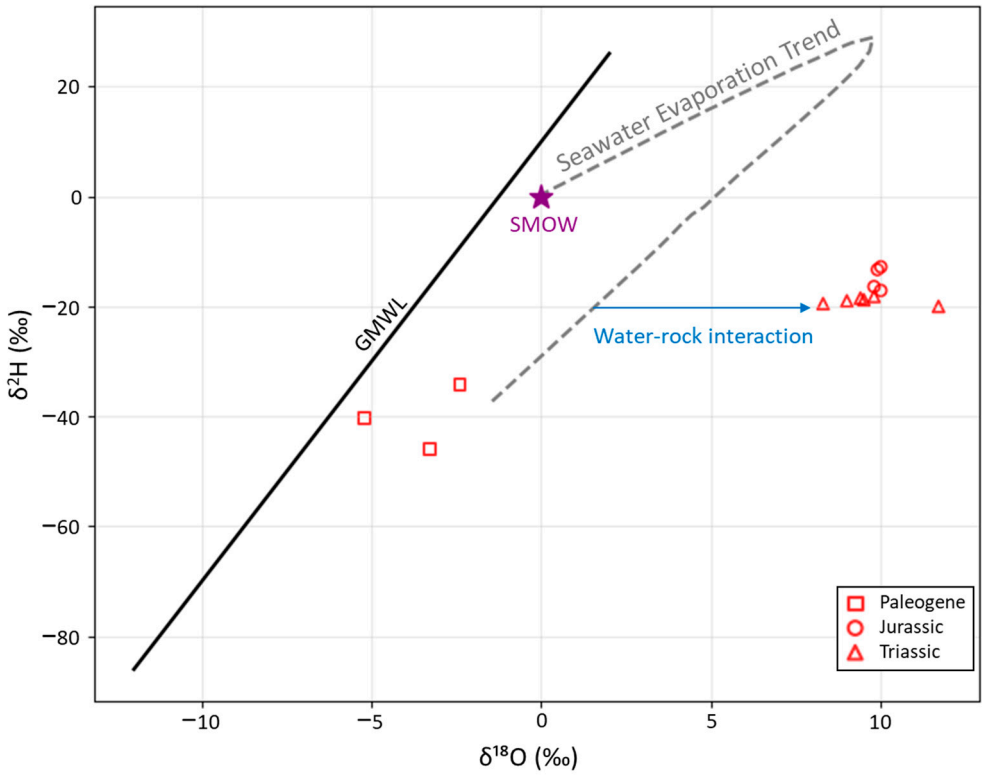


Figure 6. $\delta^{2}H$-$\delta^{18}O$ isotopic composition of brine samples from the studied aquifers, compared to the Global Meteoric Water Line (GMWL) and the Seawater Evaporation Trend [70].

6.3. Development of the Li-Prospectivity Screening Framework

To systematically identify and prioritize basinal brine systems exhibiting high Li prospectivity, we developed a multi-criteria screening framework (Figure 7). Given the highly non-linear nature of subsurface brine evolution, we adopted a convergence-of-evidence approach rather than static linear correlation coefficients; this methodology more faithfully captures the multi-phased sequence of primary evaporative concentration followed by epigenetic water–rock interaction. To ensure framework validity, the analogue datasets utilized for calibration were selected based on strict lithostratigraphical equivalence to the primary NGR aquifers, being dominated by interbedded carbonate–evaporite assemblages. This common lithological control ensures that the identified geochemical signatures are truly representative of comparable fluid–rock interactions and mineralogical boundary conditions. The framework effectively isolates the chemical and isotopic fingerprints diagnostic of subsurface Li enrichment by evaluating four integrated geochemical indicators:

- Salinity Regime and Brine Facies: The identification of hyper-saline (TDS > 100 g/L), Na-Cl hydrochemical facies establishes the essential baseline for a highly concentrated basinal brine system, which serves as a fundamental prerequisite for the accumulation of potentially elevated Li concentrations.

- Evaporation Intensity and Evolutionary Pathway: Quantitative Cl^-/Br^- mass ratios and stable water isotopes ($\delta^{18}O$ and δ^2H) are deployed to verify that the aggregate salinity is derived from the syndepositional, near-surface evaporation of seawater tracking the SET, rather than the simple subsurface dissolution of bedded halite. This maps the pristine connate brine baseline against which subsequent diagenetic modifications can be evaluated.
- Lithological Source Architecture: Because the host matrices within the primary target aquifers are predominantly pure carbonates, regional Li enrichment is contingent upon the spatial presence of intraformational or basal silicate-rich components (e.g., detrital feldspars, micas, or authigenic clay minerals) within the broader stratigraphic column. This criterion prioritizes basinal systems where hot fluids can access and aggressively leach Li from these reactive silicate phases, as the clean host carbonate matrix provides a negligible primary Li contribution. Within this architecture, dissolved B functions as an effective geochemical proxy and exploration indicator for underlying Li mineralization. Lithium and boron systematically co-occur and enrich together in deep sedimentary brines due to their shared geochemical behavior as highly incompatible lithophile elements under hydrothermal conditions [71]. This coupled enrichment signature is fundamentally rooted in the concurrent breakdown of common deep-seated source rocks and reactive mineral phases. For instance, high concentrations of both elements are frequently driven by the alteration and weathering of Li- and B-rich felsic volcanic rocks, such as ignimbrites, or liberated alongside organic-rich lithologies during deep burial maturation and hydrocarbon expulsion [10,71,72]. Crucially, under elevated thermal regimes, the diagenetic transformation of low-temperature, Li-rich clay minerals (such as smectite and montmorillonite) into the higher-temperature phase illite collapses the primary mineral frameworks, releasing significant quantities of water-soluble Li and B directly into the ambient pore water or migrating brine [5,17]. Because B partitions strongly into the aqueous phase with minimal subsequent structural re-incorporation into secondary authigenic cements, its accumulation mirrors that of conservative Li. Consequently, a pronounced anomaly in dissolved B serves as a reliable indirect signature that the fluid has actively intercepted a deep, ultra-hot silicate or volcaniclastic source architecture capable of delivering a substantial Li load to the basinal plumbing system.
- Hydrothermal Signature and Thermal Control Kinetics: The spatial convergence of anomalous B enrichments, heavy positive $\delta^{18}O$ shifts away from the SET baseline, and elevated solute-calculated paleotemperatures serves as a robust proxy for an active, high-intensity hydrothermal circulation regime. This dynamic thermal environment is thermodynamically required to break down the primary silicate frameworks and partition the mobilized Li into the co-existing aqueous phase. The validity of utilizing temperature as a primary predictive filter is uniquely substantiated by binary correlation modeling of global extra-regional analogues with known analytical chemistry (Figure 7d). When mapped on a binary coordinate system (Paleotemperature vs. Li concentration), the validation suites exhibit remarkable, near-linear positive correlations, as demonstrated by the Upper Jurassic Smackover Formation ($R^2 = 0.9052$) and the Lower Cretaceous Edwards Formation ($R^2 = 0.9697$). This striking cross-basinal consistency provides compelling empirical evidence that fluid equilibration temperature functions as a rigid thermodynamic control governing the absolute magnitude of Li partitioning and solubility during hydrothermal silicate leaching.

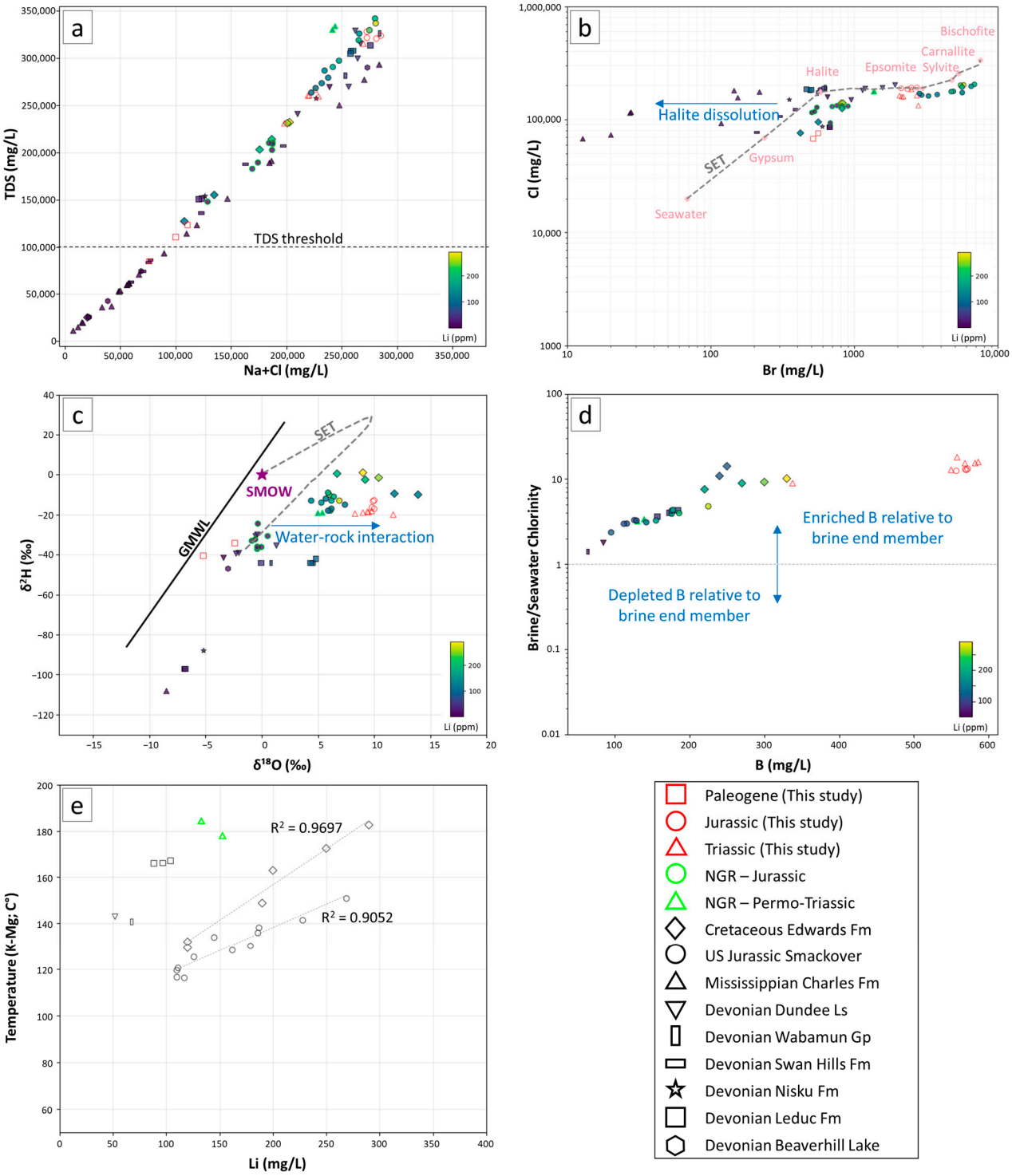


Figure 7. Stepwise filtering workflow used for validation of multi-criteria Li-prospectivity screening. At each step (**a**–**d**), samples are filtered prior to the following step as described in the text. Filters are based on: (**a**) salinity regime (TDS > 100 g/L), (**b**) evaporation intensity (Cl/Br following SET), (**c**) water–rock interaction (positive $\delta^{18}O$ shift away from SET baseline), (**d**) lithological source (enriched B relative to brine end-member as indication of presence of basal or intraformational silicates that are also potential Li sources), and (**e**) hydrothermal effect and temperature-dependent Li enrichment (the calculated temperatures are based on the (K-Mg) method [68]). Red symbols are for samples from this study. Green symbols are from published Permo-Triassic [32] and Jurassic [34] samples from the NGR. Black symbols are for non-NGR samples from North American basins [56–58] (see Table A1 for more details). The framework effectively differentiates high-prospectivity targets from low-priority systems.

By integrating these four criteria, the framework mitigates the risk of single-proxy bias and instead prioritizes target reservoirs that preserve a consistent geochemical signature across all evolutionary stages. This multidimensional approach minimizes the risk of capturing spurious geochemical correlations and yields a more reproducible, mathematically sound ranking schema than conventional single-element exploration proxies. Each individual screening criterion was systematically validated against public datasets—encompassing both NGR and non-NGR basinal aquifers—in which Li concentrations had been independently quantified. The comprehensive water chemistry and matching geothermometric calculations for these reference suites are compiled in Appendix A1, while the full validation execution is detailed visually across Figure 7. This systematic validation enables the exploration toolkit to be confidently applied to archived legacy water chemistry databases where Li was never originally analyzed.

For example, samples from the Mississippian Charles Formation were rejected as prospective targets because their Cl^-/Br^- ratios display a sharp positive deviation plotting well above the SET, indicating a salinity budget dominated by secondary halite dissolution rather than advanced primary evaporative concentration. Similarly, the Devonian Dundee Limestone was eliminated from the high-prospectivity tier due to the complete absence of any $\delta^{18}O$ enrichment relative to the SET, signaling an unperturbed, conductive thermal regime that lacked the advective hydrothermal flux required to trigger large-scale Li mobilization.

6.4. Application of the Screening Toolkit to NGR Brines

The final phase of this study involves the deployment of the newly developed screening framework across the primary analyzed samples and an expanded regional public NGR brine database to evaluate and rank their relative Li prospectivity. The results of this cross-referenced regional assessment are illustrated across Figure 7.

The Triassic and Jurassic formation water suites analyzed in this study successfully satisfy all four integrated exploration criteria. Specifically, the co-existence of high-magnitude TDS (TDS $>$ 100 g/L) within a distinct Na-Cl hydrochemical facies, clear evidence of advanced primary syndepositional evaporative evolution, and anomalously elevated B concentrations relative to the SET—which reflect a high-temperature water–rock overprint—firmly classifies these specific intervals as tier-one exploration targets with exceptional Li prospectivity.

In contrast, the Paleogene aquifer samples fail to meet the required geochemical thresholds established by the framework. Out of these three samples, one falls below the mandatory minimum TDS boundary, while the remaining two exhibit highly depleted $\delta^{18}O$ and $\delta^{2}H$ signatures. This hydrochemical configuration indicates a history dominated by massive paleometeoric dilution, which effectively flushed the reservoir and suppressed the thermodynamic and thermobaric conditions required to sustain substantial aqueous Li accumulation.

When extended to the broader NGR regional public database, the screening framework demonstrates high screening reliability and successfully distinguishes prospective horizons from unmineralized blocks. The regional Permo-Triassic basinal brines fully comply with all screening criteria, which correlate perfectly with independently reported, high-grade analytical Li concentrations of 132 to 152 mg/L [32]. This strong alignment independently validates the efficacy of the framework in identifying high-grade solute systems.

Conversely, the framework efficiently filters out and eliminates lower-priority targets across the wider basin. For instance, Middle-to-Upper Jurassic brine suites from the public NGR database [34] were screened out because they failed to exhibit the positive $\delta^{18}O$ anomalies found in our primary study samples. This distinct lack of oxygen isotope shifting marks these public datasets as structurally isolated, hydraulically stagnant basinal sectors that lacked the convective hydrothermal circulation required to drive large-scale Li mobilization, resulting in predictably low baseline Li concentrations.

While this multi-criteria screening framework provides a highly robust, mathematically sound basis for prioritizing exploration targets based on regional geochemical analogues, the definitive quantification of localized reserves ultimately requires direct physical sampling and analytical verification. In accordance with standard protocols in exploration geosciences, this predictive toolkit is designed to function as an advanced front-end de-risking mechanism. By narrowing the regional subsurface search space to the most geochemically and structurally prospective intervals, it optimizes resource allocation and maximizes the discovery probability for subsequent deep drilling and brine sampling campaigns.

7. Conclusions

This study provides a comprehensive basin-scale geochemical evaluation of subsurface brines within the NGR, successfully resolving a critical data deficit regarding Li distribution and mineralization pathways within deep carbonate–evaporite sequences. By integrating primary archived hydrochemical data with analogous global basinal datasets, we demonstrate that the high-magnitude salinity of these formation waters is fundamentally governed by primary, syndepositional seawater evaporation overprinted by subsequent deep-seated hydrothermal modifications, rather than simple in-situ congruent host-rock dissolution.

The geochemical evolution of the deep Mesozoic (Triassic and Jurassic) fluid compartments is driven by a distinct, multi-staged genetic process:

- Primary Halite-Stage Evaporation: Pristine seawater underwent intense surficial evaporation prior to burial, establishing a hyper-saline, Na-Cl connate brine backbone.
- Hydrothermal and Diagenetic Overprinting: The discovery of a pronounced isotopic decoupling—manifested as a heavy positive $\delta^{18}O$ shift without a corresponding change in $\delta^{2}H$ metrics—coincides with a massive enrichment in fluid-mobile elements (e.g., B). This independent isotopic and chemical evidence confirms an extensive hydrothermal overprint under elevated fluid-to-rock ratios.

The stark discrepancy between solute-calculated paleotemperatures and background linear conductive models demonstrates that advective upwelling of hot, deep-seated fluids, rather than static, closed-system burial diagenesis, served as the primary thermodynamic catalyst for large-scale solute mobilization. This dynamic hydrothermal regime overpassed kinetic barriers to trigger the extensive leaching of incompatible metals and metalloids from detrital frameworks within the underlying basal clastic successions, while simultaneously driving the subsurface precipitation of authigenic carbonate and anhydrite vein networks.

Synthesizing these insights facilitated the development of a multi-criteria, convergence-of-evidence screening framework anchored by four integrated exploratory indicators:

- Salinity Regime and Brine Facies: Quantitative thresholds of TDS > 100 g/L within a distinct Na-Cl hydrochemical facies.
- Evaporative Intensity and Evolutionary Pathway: Validation of halogen pathways via Cl^{-}/Br^{-} vs. trajectories and stable water isotopes.
- Lithological Source Architecture: Spatial verification of basal or intraformational reactive silicates as primary metal engines.

- Hydrothermal Fluid–Rock Signatures and Thermal Control Kinetics: Spatial convergence of boron anomalies, heavy positive $\delta^{18}O$ shifts, and elevated geothermometric thresholds, backed by verified cross-basinal binary linear correlations between fluid equilibration temperatures and absolute Li partitioning magnitudes.

Rigorous validation of this predictive tool against regional and international basinal reference suites confirms its high effectiveness in isolating high-prospectivity, hydrothermally upgraded intervals (the Triassic and Jurassic suites) from unmineralized, meteoric-flushed horizons (the Paleogene aquifer).

While this screening toolkit functions as a front-end qualitative exploration tool rather than a quantitative predictor of immediate reserves or extraction economics, it provides a highly robust, cost-effective, and scientifically sound strategy for de-risking legacy archive hydrochemical databases. By effectively narrowing the subsurface target space to specific sectors exhibiting optimal structural and geochemical fingerprints, this workflow optimizes commercial resource allocation for downstream drilling and physical sampling campaigns. Ultimately, this approach serves as a reproducible paradigm for unlocking strategic, unconventional Lithium resource frontiers within equivalent carbonate–evaporite basinal settings globally.

Author Contributions: Conceptualization, W.S.; methodology, W.S. and S.A. (Serguey Arkadakskiy); investigation, W.S., S.A. (Serguey Arkadakskiy) and S.A. (Saleh Alqahtani); writing—original draft preparation, W.S.; writing—review and editing, S.A. (Serguey Arkadakskiy) and S.A. (Saleh Alqahtani); supervision, S.A. (Saleh Alqahtani). All authors have read and agreed to the published version of the manuscript.

Funding: This research received no external funding.

Data Availability Statement: The geochemical data evaluated in this study are reported in Table 1 and Appendix A Table A1.

Acknowledgments: During preparation of this manuscript, the authors used OpenAI ChatGPT (GPT-5) to assist with language editing, manuscript re-structuring and formatting. The authors reviewed and edited the output and took full responsibility for the content.

Conflicts of Interest: The authors are employees of Saudi Aramco. The paper reflects the views of the scientists and not the company.

Appendix A

Table A1. Public geochemical datasets from NGR and non-NGR samples, along with geothermometric calculations (based on [68]).

Formation	Age	pH	TDS	Ca	Mg	Na	K	Li	Cl	SO_4	B	Br	CBE	$\delta^{18}O$ V-SMOW	$\delta^{2}H$ V-SMOW	Reference	Temp (Na,K)	Temp (K,Mg)
	Unit		mg/L	mg/L	mg/L	mg/L	mg/L	mg/L	mg/L	mg/L	mg/L	mg/L	%	‰	‰		°C	°C
NGR																		
L. Tithonian	M.-U. Jurassic	6.4	210,500	19,010	2490	54,950	2960	22	132,900	916	160	755	−2.2	−0.9	−33.1	[34]	187	149
U. Kimmeridgian	M.-U. Jurassic	6.5	208,900	17,800	2240	57,370	2850	31	130,300	972	238	700	−0.9	−0.4	−37.2	[34]	182	149
U. Kimmeridgian	M.-U. Jurassic	6.4	210,000	21,740	2660	53,120	1600	16	131,300	893	68	901	−1.1	−0.4	−36.0	[34]	152	127
L. Kimmeridgian	M.-U. Jurassic	6.7	202,600	12,570	152	59,210	1800	5	128,000	912	41	547	−5.5	−0.6	−32.4	[34]	152	183
L. Kimmeridgian	M.-U. Jurassic	6.9	189,300	11,720	1530	59,290	1810	5	115,200	1110	44	505	0.7	−0.3	−24.5	[34]	153	140
Hanifa	M.-U. Jurassic	6.6	182,700	10,120	1490	51,860	1240	16	117,500	1160	32	528	−7.0	0.5	−30.7	[34]	139	128
Dhruma	M.-U. Jurassic	6.7	147,800	15,930	1770	35,780	319	5	93,300	653	35	679	−3.0	0.0	−36.2	[34]	93	87
Kangan	Permo-Trias	5.5	333,800	26,410	2471	66,700	6420	153	177,500	252	139	1378	−4.7	5.4	−19.0	[32]	229	178
Kangan	Permo-Trias	5.4	330,000	25,910	2391	65,720	7420	133	176,000	220	130	1358	−4.8	5.0	−19.2	[32]	242	184
Non-NGR																		
Edwards	Cretaceous	5.6	232,000	17,000	1600	63,000	5800	290	140,000	2	330	810	−0.4	9.0	1.0	[57]	226	183
Edwards	Cretaceous	6.0	231,000	20,000	1600	61,000	4500	250	140,000	4	300	830	−0.2	10.4	−1.5	[57]	209	172
Edwards	Cretaceous	5.9	214,000	18,000	1500	57,000	3400	200	130,000	6	270	820	−0.7	9.2	−2.5	[57]	194	163
Edwards	Cretaceous	5.8	203,000	18,000	2900	51,000	3200	190	125,000	120	220	820	−1.3	6.7	0.5	[57]	198	149
Edwards	Cretaceous	6.1	127,000	13,000	1100	32,000	1100	120	76,000	1	250	420	1	13.9	−10.0	[57]	159	129
Edwards	Cretaceous	6.2	155,000	14,000	1300	40,000	1300	120	95,000	2	240	560	−1.2	11.8	−9.5	[57]	156	132
Edwards	Cretaceous	6.5	25,200	1900	580	6500	130	8	14,000	1700	15	82	−1.1	−3.6	−24.5	[57]	130	79
Smackover	Jurassic	4.6	341,953	43,275	4538	75,625	2928	187	204,588	117	155	6856	0.9	6.4	−11.0	[58]	166	138
Smackover	Jurassic	5.4	336,832	38,700	3445	78,525	3690	269	202,307	128	225	5763	0.1	6.9	−13.0	[58]	178	151
Smackover	Jurassic	5.4	329,551	38,848	3332	73,803	2765	228	201,355	158	186	5487	−1.8	6.0	−10.0	[58]	164	141
Smackover	Jurassic	5.6	318,872	38,159	3521	71,713	2409	186	193,784	151	176	5626	−1	5.9	−9.0	[58]	158	136
Smackover	Jurassic	5.5	297,251	35,550	3810	70,350	1980	162	177,348	172	176	4893	1.7	6.2	−13.0	[58]	148	128
Smackover	Jurassic	5.6	290,516	35,303	3177	65,636	1918	179	176,461	157	178	4726	−0.7	6.1	−18.0	[58]	150	130
Smackover	Jurassic	5.0	286,735	37,800	3948	61,700	1835	126	172,926	190	95	5637	0.3	4.4	−13.0	[58]	151	125
Smackover	Jurassic	5.3	325,878	43,100	4288	69,250	2505	145	196,703	132	142	6501	0	5.3	−14.0	[58]	162	134
Smackover	Jurassic	5.8	268,250	31,181	2686	62,003	1255	110	164,562	101	126	2939	−1.2	5.7	−12.0	[58]	130	119
Smackover	Jurassic	6.2	273,356	30,135	2709	65,706	1130	117	166,384	110	116	3774	−0.8	6.2	−17.0	[58]	122	116
Smackover	Jurassic	5.7	263,403	30,478	2629	61,063	1125	110	161,597	147	112	3281	−1.4	5.9	−18.0	[58]	126	117
Smackover	Jurassic	5.6	279,162	30,800	2735	67,600	1310	111	170,302	166	129	2837	−0.5	7.4	−15.0	[58]	128	121
Charles	Mississippian	6.3	277,000	6340	859	95,500	2260	25	175,000	518	176	218	−3.6	−4.6	−93.8	[57]	139	158
Charles	Mississippian	7.8	52,400	1100	203	18,300	510	19	31,100	2210	133	72	−2.5	−10.6	−112.7	[57]	147	132
Charles	Mississippian	6.5	250,000	3700	457	92,000	1670	17	156,000	512	108	154	−1.6	−6.3	−103.3	[57]	125	159

Table A1. *Cont.*

Formation	Age	pH	TDS	Ca	Mg	Na	K	Li	Cl	SO_4	B	Br	CBE	$\delta^{18}O$ V-SMOW	$\delta^{2}H$ V-SMOW	Reference	Temp (Na,K)	Temp (K,Mg)
	Unit		mg/L	mg/L	mg/L	mg/L	mg/L	mg/L	mg/L	mg/L	mg/L	mg/L	%	‰	‰		°C	°C
Charles	Mississippian	6.3	293,000	3870	451	104,000	1590	16	180,000	482	100	145	−2.9	−8.5	−108.0	[57]	117	157
Charles	Mississippian	6.2	151,000	3390	477	54,500	1350	16	92,500	877	92	118	−0.3	−10.3	−112.1	[57]	141	150
Charles	Mississippian	8.1	37,000	587	96.6	16,700	427	13	25,700	2790	126	42	−0.8	−11.7	−115.8	[57]	143	138
Charles	Mississippian	8.1	19,900	280	52.2	6440	152	10	9220	3100	49	16	−4.3	−15.0	−129.7	[57]	138	115
Charles	Mississippian	6.6	191,000	1670	221	70,800	640	8	116,000	1500	40	28	−1.6	−14.2	−148.3	[57]	93	138
Charles	Mississippian	7.3	19,400	439	84	6290	226	8	10,200	1920	37.3	18	−3.8	−16.3	−130.9	[57]	162	120
Charles	Mississippian	6.6	189,000	1650	217	70,900	632	8	114,000	1500	40	27	−0.7	−14.2	−145.1	[57]	93	138
Charles	Mississippian	7.4	14,900	382	60	4940	165	6	7220	1760	14.8	9	−0.3	−17.8	−137.8	[57]	158	116
Charles	Mississippian	7.7	61,500	886	120	22,300	473	6	36,000	1530	12.4	11	−0.5	−17.6	−130.1	[57]	133	138
Charles	Mississippian	7.7	59,700	879	130	21,000	482	5	35,300	1600	12.4	17	−2.6	−17.0	−136.1	[57]	137	137
Charles	Mississippian	7.6	52,900	804	120	17,800	405	5	31,000	1370	12.7	15	−4.1	−17.2	−136.4	[57]	137	133
Charles	Mississippian	7.6	53,600	807	122	18,500	412	5	31,700	1500	12.2	15	−3.5	−17.3	−136.9	[57]	135	133
Charles	Mississippian	6.8	61,200	688	94	22,600	376	5	35,600	1710	12.2	8	−0.2	−18.0	−136.0	[57]	121	134
Charles	Mississippian	6.8	60,900	685	94	22,500	376	5	35,400	1710	11.6	8	−0.2	−17.9	−138.0	[57]	121	134
Charles	Mississippian	7.5	70,600	737	107	25,100	487	5	42,000	1770	14	15	−3.1	−17.1	−135.1	[57]	128	141
Charles	Mississippian	7.8	11,100	239	38	3540	78.7	5	4190	2400	9	6	−1.8	−17.8	−137.6	[57]	135	101
Charles	Mississippian	6.8	114,000	1030	155	42,500	527	5	67,600	1890	16	13	−0.5	−17.3	−138.9	[57]	107	137
Charles	Mississippian	7.7	59,500	651	93	21,100	381	5	35,300	1770	12	11	−3.4	−17.3	−137.7	[57]	125	135
Charles	Mississippian	7.1	93,100	881	134	34,100	462	5	55,700	1760	14	17	−1.9	−16.9	−138.6	[57]	111	135
Charles	Mississippian	7.6	123,000	948	145	46,400	521	5	73,000	1940	17	20	−0.2	−16.5	−136.0	[57]	103	138
Charles	Mississippian	6.8	35,900	793	139	12,600	276	4	21,200	1430	10	11	−2.1	−17.6	−139.3	[57]	135	118
Dundee	Devonian	5.0	328,880	51,800	6880	60,400	4160	52	202,000	103	84	1920	1.7	1.3	−35.5	[57]	204	143
Dundee	Devonian	5.5	315,206	36,400	5790	76,100	3010	44	191,000	160	31	1570	2.7	−0.5	−30.8	[57]	168	135
Dundee	Devonian	5.3	269,534	32,000	5080	68,400	2540	44	188,000	118	47	1190	−2.3	−0.4	−30.0	[57]	164	132
Dundee	Devonian	5.2	299,414	26,000	5070	83,500	1870	33	181,000	137	8	1140	2.7	−2.0	−39.2	[57]	136	122
Dundee	Devonian	5.9	240,643	23,000	4420	61,300	920	24	149,000	189	6	950	0	−2.3	−39.5	[57]	116	103
Dundee	Devonian	5.1	269,155	16,000	5320	81,100	520	2	158,000	20	1	650	3.5	−3.4	−41.6	[57]	79	86
Wabamun Gp	Devonian	6.5	281,637	25,266	4300	80,551	2318	48	172,691	985	62	549	2.8	−0.2	−45.0	[56]	149	131
Wabamun Gp	Devonian	6.3	326,306	29,803	4406	91,059	3133	68	193,192	836	63	622	3.6	0.8	−44.0	[56]	159	141
Swan Hills	Devonian	6.7	187,656	9997	1340	56,297	1106	29	106,785	972	68	303	0.8	−2.4	−62.0	[56]	129	126
Swan Hills	Devonian	7.1	136,000	6593	968	45,805	729	19	77,466	1197	47	208	4.4	−4.1	−74.0	[56]	119	118
Swan Hills	Devonian	6.3	207,015	3894	615	74,078	1902	36	123,090	560	158	386	0.4	5.0	−50.0	[56]	143	158
Swan Hills	Devonian	7.3	62,953	1545	240	23,803	449	9	35,705	1775	42	49	4.3	−11.4	−116.0	[56]	127	125
Swan Hills	Devonian	7.1	83,556	2363	327	28,907	696	14	46,737	1161	56	127	2.6	−10.8	−112.0	[56]	140	134
Swan Hills	Devonian	7.5	74,269	2150	325	28,113	472	11	42,485	1888	43	113	4.7	−8.4	−99.0	[56]	121	122
Swan Hills	Devonian	7.3	86,381	2429	338	29,251	708	14	47,837	1162	56	140	2.1	−10.5	−110.0	[56]	140	134
Nisku	Devonian	6.5	257,175	17,259	3063	77,381	949	25	149,733	983	40	352	2.9	1.5	−37.0	[56]	106	109
Nisku	Devonian	6.7	153,720	14,054	2295	40,187	1757	31	86,522	1098	79	598	4.0	−5.2	−88.0	[56]	174	133
Leduc	Devonian	7.0	307,824	32,648	4163	76,140	6355	104	181,896	9223	184	489	1.0	4.5	−44.0	[56]	218	167
Leduc	Devonian	6.5	151,386	16,345	2600	37,627	1755	29	86,115	1316	79	668	4.7	−6.9	−97.0	[56]	178	130

Table A1. *Cont.*

Formation	Age	pH	TDS	Ca	Mg	Na	K	Li	Cl	SO_4	B	Br	CBE	$\delta^{18}O$ V-SMOW	$\delta^{2}H$ V-SMOW	Reference	Temp (Na,K)	Temp (K,Mg)
	Unit		mg/L	mg/L	mg/L	mg/L	mg/L	mg/L	mg/L	mg/L	mg/L	mg/L	%	‰	‰		°C	°C
Leduc	Devonian	6.6	150,563	15,606	2506	34,619	1649	29	86,381	1319	79	670	1.1	−6.8	−97.0	[56]	179	129
Leduc	Devonian	6.5	313,560	29,250	4469	86,229	2504	47	189,540	1170	61	615	2.4	−0.1	−44.0	[56]	150	133
Leduc	Devonian	6.9	308,088	33,143	3863	75,738	5963	97	184,386	8776	173	498	0.2	4.8	−42.0	[56]	214	166
Leduc	Devonian	6.9	304,848	31,886	3703	71,949	5828	88	185,712	15,184	157	460	−3.7	4.3	−44.0	[56]	216	166
Beaverhill Lake Group	Devonian	7.6	74,164	2004	325	27,064	451	11	41,960	1574	40	114	3.7	−8.2	−98.0	[56]	121	120
Beaverhill Lake Group	Devonian	7.5	25,552	1313	237	7696	80	2	14,252	1252	7	34	−1.4	−12.5	−114.0	[56]	99	78
Beaverhill Lake Group	Devonian	7.5	25,348	1344	242	7910	83	2	13,743	1252	7	35	1.7	−12.5	−113.0	[56]	100	78
Beaverhill Lake Group	Devonian	6.2	289,912	21,977	2338	88,610	1087	23	184,702	818	25	573	−0.6	−3.0	−47.0	[56]	107	117
Beaverhill Lake Group	Devonian	7.9	42,559	579	74	15,420	609	8	23,541	308	39	49	3.0	−8.6	−119.0	[56]	168	155

References

1. Fortier, S.M.; Hammarstrom, J.M.; Ryker, S.J.; Day, W.C.; Seal, R.R. *USGS Critical Minerals Review*; U.S. Geological Survey: Reston, VA, USA, 2025. Available online: https://www.usgs.gov/publications/usgs-critical-minerals-review (accessed on 20 October 2026).
2. Bustos-Gallardo, B.; Bridge, G.; Prieto, M. Harvesting Lithium: Water, Brine and the Industrial Dynamics of Production in the Salar de Atacama. *Geoforum* **2021**, *119*, 177–189. [CrossRef]
3. Dugamin, E.J.M.; Cathelineau, M.; Boiron, M.-C.; Richard, A.; Despinois, F. Lithium Enrichment Processes in Sedimentary Formation Waters. *Chem. Geol.* **2023**, *635*, 121626. [CrossRef]
4. Stringfellow, W.T.; Dobson, P.F. Technology for the Recovery of Lithium from Geothermal Brines. *Energies* **2021**, *14*, 6805. [CrossRef]
5. Williams, L.B.; Środoń, J.; Huff, W.D.; Clauer, N.; Hervig, R.L. Light Element Distributions (N, B, Li) in Baltic Basin Bentonites Record Organic Sources. *Geochim. Cosmochim. Acta* **2013**, *120*, 582–599. [CrossRef]
6. Williams, L.B.; Crawford Elliott, W.; Hervig, R.L. Tracing Hydrocarbons in Gas Shale Using Lithium and Boron Isotopes: Denver Basin USA, Wattenberg Gas Field. *Chem. Geol.* **2015**, *417*, 404–413. [CrossRef]
7. Munk, L.A.; Hynek, S.A.; Bradley, D.C.; Boutt, D.; Labay, K.; Jochens, H. Lithium Brines: A Global Perspective. In *Rare Earth and Critical Elements in Ore Deposits*; Verplanck, P.L., Hitzman, M.W., Eds.; Society of Economic Geologists: Littleton, CO, USA, 2016; pp. 339–365. ISBN 978-1-62949-218-6.
8. Lee, K.J. Potential of Petroleum Source Rock Brines as a New Source of Lithium: Insights from Basin-Scale Modeling and Local Sensitivity Analysis. *Energy Rep.* **2022**, *8*, 56–68. [CrossRef]
9. Yan, K.; Wang, C.; Chen, R.; Liu, C.; Wang, J.; Yu, X.; Shen, L.; Li, R.; Zhou, Y.; Zhou, Q. Origin and Evolution of Deep Lithium-Rich Brines in the Southwest Jianghan Basin, Central China: Evidence from Hydrochemistry and Stable Isotopes. *J. Hydrol.* **2023**, *626*, 130163. [CrossRef]
10. Lee, K.J.; You, J.; Gao, Y.; Terlier, T. Release, Transport, and Accumulation of Lithium in Shale Brines. *Fuel* **2024**, *356*, 129629. [CrossRef]
11. Butler, K.L.; Munk, L.A.; Boutt, D.F.; Morris, N.; Kennedy, J.; Saha, P.; Blake, M.R.; Custado, M.J.; Ibarra, D.E. The Origin and Enrichment of Sedimentary Basin Lithium Brines: A Case Study From the Upper Devonian Leduc Formation, Alberta Basin, Canada. *Econ. Geol.* **2025**, *120*, 649–662. [CrossRef]
12. Saeed, W. Sources and Mechanism of Lithium Enrichment in Oilfield Brines. In *Proceedings of the Middle East Oil, Gas and Geosciences Show (MEOS GEO)*; SPE: Manama, Bahrain, 2025; p. D011S032R005.
13. Williams, G.D.Z.; Vengosh, A. Origins of the Mg/Li Ratio in Closed-Basin Brines of the Lithium Triangle: The Relative Importance of High- and Low-Temperature Water-Rock Interactions. *Earth-Sci. Rev.* **2026**, *278*, 105516. [CrossRef]
14. Ruggieri, F.; Saavedra, J.; Fernandez-Turiel, J.L.; Gimeno, D.; Garcia-Valles, M. Environmental Geochemistry of Ancient Volcanic Ashes. *J. Hazard. Mater.* **2010**, *183*, 353–365. [CrossRef] [PubMed]
15. Luo, M.; Yu, M.; Torres, M.E.; Solomon, E.A.; Gieskes, J.; You, C.-F.; Kong, L.; Chen, D. Volcanic Ash Alteration Triggers Active Sedimentary Lithium Cycling: Insights from Lithium Isotopic Compositions of Pore Fluids and Sediments in the Hikurangi Subduction Zone. *Earth Planet. Sci. Lett.* **2024**, *642*, 118854. [CrossRef]
16. Benson, T.R.; Coble, M.A.; Rytuba, J.J.; Mahood, G.A. Lithium Enrichment in Intracontinental Rhyolite Magmas Leads to Li Deposits in Caldera Basins. *Nat. Commun.* **2017**, *8*, 270. [CrossRef] [PubMed]
17. Phan, T.T.; Capo, R.C.; Stewart, B.W.; Macpherson, G.L.; Rowan, E.L.; Hammack, R.W. Factors Controlling Li Concentration and Isotopic Composition in Formation Waters and Host Rocks of Marcellus Shale, Appalachian Basin. *Chem. Geol.* **2016**, *420*, 162–179. [CrossRef]
18. Huff, G.F. *Origin and Li-Enrichment of Selected Oilfield Brines in the Alberta Basin, Canada*; Alberta Geological Survey: Edmonton, AB, Canada; Alberta Energy Regulator: Calgary, AB, Canada, 2019.
19. Barton, C.A.; Zoback, M.D.; Moos, D. Fluid Flow along Potentially Active Faults in Crystalline Rock. *Geology* **1995**, *23*, 683–686. [CrossRef]
20. Zoback, M.D. *Reservoir Geomechanics*; Cambridge University Press: Cambridge, UK, 2007; ISBN 978-0-521-14619-7.
21. Evans, J.P.; Forster, C.B.; Goddard, J.V. Permeability of Fault-Related Rocks, and Implications for Hydraulic Structure of Fault Zones. *J. Struct. Geol.* **1997**, *19*, 1393–1404. [CrossRef]
22. Coffey, D.M.; Munk, L.A.; Ibarra, D.E.; Butler, K.L.; Boutt, D.F.; Jenckes, J. Lithium Storage and Release From Lacustrine Sediments: Implications for Lithium Enrichment and Sustainability in Continental Brines. *Geochem. Geophys. Geosyst.* **2021**, *22*, e2021GC009916. [CrossRef]
23. Li, Q.; Fan, Q.; Wang, J.; Qin, Z.; Zhang, X.; Wei, H.; Du, Y.; Shan, F. Hydrochemistry, Distribution and Formation of Lithium-Rich Brines in Salt Lakes on the Qinghai-Tibetan Plateau. *Minerals* **2019**, *9*, 528. [CrossRef]
24. Huff, D.E.; Holley, E.A.; Guenthner, W.R. Igneous Geochronology and Thermochronology of the Northern Battle Mountain District, Nevada: Implications for Gold Mineralization. *Econ. Geol.* **2025**, *120*, 137–169. [CrossRef]

25. Nelson, S.T.; Mayo, A.L.; Gilfillan, S.; Dutson, S.J.; Harris, R.A.; Shipton, Z.K.; Tingey, D.G. Enhanced Fracture Permeability and Accompanying Fluid Flow in the Footwall of a Normal Fault: The Hurricane Fault at Pah Tempe Hot Springs, Washington County, Utah. *GSA Bull.* **2009**, *121*, 236–246. [CrossRef]
26. Kettermann, M.; Urai, J.L.; Vrolijk, P.J. Evolution of Structure and Permeability of Normal Faults with Clay Smear: Insights from Water-saturated Sandbox Models and Numerical Simulations. *J. Geophys. Res. Solid Earth* **2017**, *122*, 1697–1725. [CrossRef]
27. Stern, R.J.; Johnson, P. Continental Lithosphere of the Arabian Plate: A Geologic, Petrologic, and Geophysical Synthesis. *Earth-Sci. Rev.* **2010**, *101*, 29–67. [CrossRef]
28. Stern, R.J. The Najd Fault System, Saudi Arabia and Egypt: A Late Precambrian Rift-Related Transform System? *Tectonics* **1985**, *4*, 497–511. [CrossRef]
29. Wilson, A.O. Chapter 1 Introduction to the Jurassic Arabian Intrashelf Basin. *Geol. Soc. Lond. Mem.* **2020**, *53*, 1–19. [CrossRef]
30. Alsharhan, A.S.; Nairn, A.E.M. *Sedimentary Basins and Petroleum Geology of the Middle East*; Elsevier: Amsterdam, The Netherlands, 2003; ISBN 978-0-444-82465-3.
31. Saeed, W.; Shouakar-Stash, O.; Unger, A.; Wood, W.W.; Parker, B. Origin of Solutes in a Regional Multi-Layered Sedimentary Aquifer System (a Case Study from the Rub' al Khali Basin, Saudi Arabia). *Appl. Geochem.* **2021**, *126*, 104871. [CrossRef]
32. Bagheri, R.; Nadri, A.; Raeisi, E.; Shariati, A.; Mirbagheri, M.; Bahadori, F. Chemical Evolution of a Gas-Capped Deep Aquifer, Southwest of Iran. *Environ. Earth Sci.* **2014**, *71*, 3171–3180. [CrossRef]
33. English, K.L.; English, J.M.; Redfern, J.; Hollis, C.; Corcoran, D.V.; Oxtoby, N.; Yahia Cherif, R. Remobilization of Deep Basin Brine during Exhumation of the Illizi Basin, Algeria. *Mar. Pet. Geol.* **2016**, *78*, 679–689. [CrossRef]
34. Birkle, P.; Zayer, A.J. Provenance of Oilfield Brines and Vertical Connectivity of Middle to Upper Jurassic Sequence in Eastern Saudi Arabia. *Appl. Geochem.* **2026**, *197*, 106673. [CrossRef]
35. Beydoun, Z.R. The Petroleum Resources of the Middle East: A Review. *J. Pet. Geol.* **1986**, *9*, 5–27. [CrossRef]
36. Christian, L. Cretaceous Subsurface Geology of the Middle East Region. *GeoArabia* **1997**, *2*, 239–256. [CrossRef]
37. Martin, A.Z. Late Permian to Holocene Paleofacies Evolution of the Arabian Plate and Its Hydrocarbon Occurrences. *GeoArabia* **2001**, *6*, 445–504. [CrossRef]
38. Scotese, C.R. *PALEOMAP PaleoAtlas for GPlates and the PaleoData Plotter Program*; PALEOMAP Project: Evanston, IL, USA, 2016. Available online: http://www.earthbyte.org/paleomap-paleoatlas-for-gplates/ (accessed on 8 July 2026).
39. Müller, R.D.; Cannon, J.; Qin, X.; Watson, R.J.; Gurnis, M.; Williams, S.; Pfaffelmoser, T.; Seton, M.; Russell, S.H.J.; Zahirovic, S. GPlates: Building a Virtual Earth Through Deep Time. *Geochem. Geophys. Geosyst.* **2018**, *19*, 2243–2261. [CrossRef]
40. Drysdall, A.R.; Douch, C.J. NbThZr Mineralization in Microgranite—Microsyenite at Jabal Tawlah, Midyan Region, Kingdom of Saudi Arabia. *J. Afr. Earth Sci. 1983* **1986**, *4*, 275–288. [CrossRef]
41. Azer, M.K.; Gahlan, H.A.; Bartoli, O. Formation of Li-Bearing Pegmatites in the Arabian Shield: A Case Study from the Mount Ablah, Asir Terran, Saudi Arabia. *Environ. Earth Sci.* **2025**, *84*, 305. [CrossRef]
42. Ramsay, C.R. Specialized Felsic Plutonic Rocks of the Arabian Shield and Their Precursors. *J. Afr. Earth Sci. 1983* **1986**, *4*, 153–168. [CrossRef]
43. Küster, D. Granitoid-Hosted Ta Mineralization in the Arabian–Nubian Shield: Ore Deposit Types, Tectono-Metallogenetic Setting and Petrogenetic Framework. *Ore Geol. Rev.* **2009**, *35*, 68–86. [CrossRef]
44. Akal, C.; Candan, O.; Koralay, O.E.; Gerdes, A.; Oberhaensli, R. Middle Triassic Magmatism in the Afyon Zone of the Anatolides/Eastern Mediterranean: Implications for the Extension of the Northern Margin of Gondwana and Opening of the Inner-Tauride Ocean. *Lithos* **2024**, *482–483*, 107691. [CrossRef]
45. Chauvet, F.; Lapierre, H.; Maury, R.C.; Bosch, D.; Basile, C.; Cotten, J.; Brunet, P.; Campillo, S. Triassic Alkaline Magmatism of the Hawasina Nappes: Post-Breakup Melting of the Oman Lithospheric Mantle Modified by the Permian Neotethyan Plume. *Lithos* **2011**, *122*, 122–136. [CrossRef]
46. Deevsalar, R.; Shinjo, R.; Liégeois, J.P.; Valizadeh, M.V.; Ahmadian, J.; Yeganehfar, H.; Murata, M.; Neill, I. Subduction-Related Mafic to Felsic Magmatism in the Malayer–Boroujerd Plutonic Complex, Western Iran. *Swiss J. Geosci.* **2018**, *111*, 269–293. [CrossRef]
47. Franz, G.; Harms, U.; Denkler, T. Late Cretaceous Igneous Activity in the Delgo Uplift (Northern Province, Sudan). In *Geoscientific Research in Northeast Africa*; Thorweihe, U., Schandelmeier, H., Eds.; Balkema: Rotterdam, The Netherlands, 1993; pp. 227–230, ISBN 978-0-203-75339-2.
48. Bosworth, W.; Huchon, P.; McClay, K. The Red Sea and Gulf of Aden Basins. *J. Afr. Earth Sci.* **2005**, *43*, 334–378. [CrossRef]
49. Azizi, H.; Stern, R.J. Jurassic Igneous Rocks of the Central Sanandaj–Sirjan Zone (Iran) Mark a Propagating Continental Rift, Not a Magmatic Arc. *Terra Nova* **2019**, *31*, 415–423. [CrossRef]
50. Ortiz, M.A.; Vahrenkamp, V. Lithium Potential in Saudi Arabia—An Initial Assessment. In *Proceedings of the Middle East Oil, Gas and Geosciences Show (MEOS GEO)*; SPE: Manama, Bahrain, 2025; p. D011S032R001.

51. Deville De Periere, M.; Mangenot, X.; Dyja-Person, V.; Muslem, A. Diagenetic Control on Rock-Type Heterogeneity in Dolomitized Upper Triassic Jilh Formation (Saudi Arabia) Revealed by In-Situ LA-ICP-MS U/Pb Dating. In *Proceedings of the Middle East Oil, Gas and Geosciences Show (MEOS GEO)*; SPE: Manama, Bahrain, 2025; p. D021S074R001.
52. Cantrell, D.L.; Swart, P.K.; Handford, R.C.; Kendall, C.G.; Westphal, H. Geology and Production Significance of Dolomite, Arab-D Reservoir, Ghawar Field, Saudi Arabia. *GeoArabia* **2001**, *6*, 45–60. [CrossRef]
53. Swart, P.K.; Cantrell, D.L.; Westphal, H.; Handford, C.R.; Kendall, C.G. Origin of Dolomite in the Arab-D Reservoir from the Ghawar Field, Saudi Arabia: Evidence from Petrographic and Geochemical Constraints. *J. Sediment. Res.* **2005**, *75*, 476–491. [CrossRef]
54. Al-Hajeri, M.M.; Parnell, J.; Bowden, S.; Costanzo, A.; Feely, M. Deep Hydrothermal Activity in Hydrocarbon Reservoirs, South Kuwait. *Arab. J. Geosci.* **2017**, *10*, 41. [CrossRef]
55. Arouri, K.R.; Alqahtani, S.A. Fluid Characterization of Oil and Gas Fields: Implications for Fault and Top Seal Integrity Assessment. *Pet. Geosci.* **2024**, *30*, petgeo2023-068. [CrossRef]
56. Reimert, C.; Lyster, S.; Palombi, D.; Bernal, N. *Brine Geochemical Data, Mineral Mapping Program, 2021–2024 (Tabular Data, Tab-Delimited Format)*; Alberta Energy Regulator: Calgary, AB, Canada, 2025.
57. Blondes, M.S.; Knierim, K.J.; Croke, M.R.; Freeman, P.A.; Doolan, C.; Herzberg, A.S.; Shelton, J.L. U.S. Geological Survey National Produced Waters Geochemical Database (Ver. 3.0, December 2023). Available online: https://catalog.data.gov/dataset/u-s-geological-survey-national-produced-waters-geochemical-database-ver-3-0-december-2023 (accessed on 9 April 2026).
58. Moldovanyi, E.P.; Walter, L.M. Regional Trends in Water Chemistry, Smackover Formation, Southwest Arkansas: Geochemical and Physical Controls. *AAPG Bull.* **1992**, *76*, 864–894. [CrossRef]
59. Mirnejad, H.; Sisakht, V.; Mohammadzadeh, H.; Amini, A.H.; Rostron, B.J.; Haghparast, G. Major, Minor Element Chemistry and Oxygen and Hydrogen Isotopic Compositions of Marun Oil-field Brines, SW Iran: Source History and Economic Potential. *Geol. J.* **2011**, *46*, 1–9. [CrossRef]
60. Carpenter, A.B. Origin And Chemical Evolution Of Brines In Sedimentary Basins. In *Proceedings of the SPE Annual Fall Technical Conference and Exhibition*; SPE: Houston, TX, USA, 1978; p. SPE-7504-MS.
61. Mansurbeg, H.; Alsuwaidi, M.; Dong, S.; Shahrokhi, S.; Morad, S. Origin of Drusy Dolomite Cement in Permo-Triassic Dolostones, Northern United Arab Emirates. *Water* **2021**, *13*, 1908. [CrossRef]
62. Gerritse, R.G.; George, R.J. The Role of Soil Organic Matter in the Geochemical Cycling of Chloride and Bromide. *J. Hydrol.* **1988**, *101*, 83–95. [CrossRef]
63. Matray, J.-M. Hydrochimie et Géochime Isotopiques des Eaux de Réservoir Pétrolier du Trias et du Dogger Dans le Bassin de Paris. Ph.D. Thesis, Université de Paris XI, Paris, France, 1988.
64. Rittenhouse, G. Bromine in Oil-Field Waters and Its Use in Determining Possibilities of Origin of These Waters. *AAPG Bull.* **1967**, *51*, 2430–2440. [CrossRef]
65. Clark, I.D.; Fritz, P. *Environmental Isotopes in Hydrogeology*; CRC Press: Boca Raton, FL, USA, 2013; ISBN 978-0-429-06957-4.
66. Rolandone, F.; Lucazeau, F.; Leroy, S.; Mareschal, J.-C.; Jorand, R.; Goutorbe, B.; Bouquerel, H. New Heat Flow Measurements in Oman and the Thermal State of the Arabian Shield and Platform. *Tectonophysics* **2013**, *589*, 77–89. [CrossRef]
67. Salisu, A.M.; Bello, A.M.; Amao, A.O.; Al-Ramadan, K. The Role of Fluid Chemistry in the Diagenetic Transformation of Detrital Clay Minerals: Experimental Insights from Modern Estuarine Sediments. *Minerals* **2025**, *15*, 317. [CrossRef]
68. Giggenbach, W.F. Geothermal Solute Equilibria. Derivation of Na-K-Mg-Ca Geoindicators. *Geochim. Cosmochim. Acta* **1988**, *52*, 2749–2765. [CrossRef]
69. Hanor, J.S.; McIntosh, J.C. Are Secular Variations in Seawater Chemistry Reflected in the Compositions of Basinal Brines? *J. Geochem. Explor.* **2006**, *89*, 153–156. [CrossRef]
70. Holser, W.T. Chapter 9. Trace Elements and Isotopes in Evaporites. In *Marine Minerals*; Burns, R.G., Ed.; Mineralogical Society of America: Washington, DC, USA, 1979; Volume 6, pp. 295–346, ISBN 978-0-939950-06-5.
71. Williams, G.D.Z.; Nativ, P.; Vengosh, A. The Role of Boron in Controlling the pH of Lithium Brines. *Sci. Adv.* **2025**, *11*, eadw3268. [CrossRef] [PubMed]
72. Risacher, F.; Fritz, B. Origin of Salts and Brine Evolution of Bolivian and Chilean Salars. *Aquat. Geochem.* **2009**, *15*, 123–157. [CrossRef]

Disclaimer/Publisher's Note: The statements, opinions and data contained in all publications are solely those of the individual author(s) and contributor(s) and not of MDPI and/or the editor(s). MDPI and/or the editor(s) disclaim responsibility for any injury to people or property resulting from any ideas, methods, instructions or products referred to in the content.